NOVEL MINIATURIZED SENSORS FOR ON-SITE BIOLOGICAL AND CHEMICAL DETECTION

A DISSERTATION SUBMITTED TO

THE GRADUATE SCHOOL OF ENGINEERING AND SCIENCE

OF BILKENT UNIVERSITY

IN PARTIAL FULFILLMENT OF THE REQUIREMENTS FOR

THE DEGREE OF

DOCTOR OF PHILOSOPHY

IN

MATERIALS SCIENCE AND NANOTECHNOLOGY

By

Hasan Güner

August 2016

NOVEL MINIATURIZED SENSORS FOR ON-SITE BIOLOGICAL AND CHEMICAL DETECTION

By Hasan Güner

August 2016

We certify that we have read this dissertation and that in our opinion it is fully adequate, in scope and in quality, as a dissertation for the degree of Doctor of Philosophy.

Aykutlu Dana(Advisor)

Ali Kemal Okyay

Mehmet Özgür Öktel

Adil Denizli

Hamza Kurt

Approved for the Graduate School of Engineering and Science:

Levent Onural
Director of the Graduate School

ABSTRACT

NOVEL MINIATURIZED SENSORS FOR ON-SITE BIOLOGICAL AND CHEMICAL DETECTION

Hasan Güner
Ph.D. in Materials Science and Nanotechnology
Advisor: Aykutlu Dana
August 2016

The development of miniaturized analytical systems brought several examples of novel platforms for a variety of applications in medical diagnostics, food safety, biodefense, agricultural and environmental monitoring. Portability, sensitivity, reliability, short turn-around-time, cost-efficiency and connectivity are some of the critical assets that successful devices should possess. The advancements in such areas enabled the detection and analysis of biological and chemical agents outside the laboratory settings. In this thesis, we focus on the development of miniaturized sensor designs for on-site biological and chemical detection utilizing surface plasmon resonance sensing and infrared absorption spectroscopy. We proposed an integrated refractometric sensor combining a grating-coupled plasmon resonance surface with a planar photodiode which can find applications in lab-on-a-chip designs with high integration density. In order to address the use of lab-on-a-chip systems in point-of-care testing applications, we have developed a surface plasmon resonance imaging platform integrated with a smartphone. We have fabricated low cost and sensitive grating coupled surface plasmon resonance sensor chips using off-the-shelf optical storage discs. Then we have experimentally shown the capability of multiplexed detection and biomolecular sensing. Finally, we demonstrated infrared absorption spectroscopy on a mobile phone by developing a compact mid-infrared spectrometer that hosts a miniature uncooled thermal camera and a custom-designed silicon transmission diffraction grating.

Keywords: Miniature sensors, analytical systems, lab-on-a-chip devices, surface plasmon resonance sensing, infrared absorption spectroscopy, mobile phone based sensing.

ÖZET

YERİNDE BİYOLOJİK VE KİMYASAL TAYİNİNE YÖNELİK YENİ MİNYATÜR ALGILAYICILAR

Hasan Güner
Malzeme Bilimi ve Nanoteknoloji, Doktora
Tez Danışmanı: Aykutlu Dana
Ağustos 2016

Minyatür analitik sistemlerdeki gelişmeler, tıbbi tanı, gıda güvenliği, biyosavunma, zırai ve çevresel tarama uygulamalarına yönelik yeni platformları beraberinde getirdi. Bu bağlamdaki başarılı bir cihazdan beklenen başlıca nitelikler arasında taşınabilirlik, hassasiyet, güvenilirlik, kısa sürede sonuç türetebilme, maliyet avantajı ve bağlanabilirlik özellikleri sayılabilir. Bu alanlardaki ilerlemeler sayesinde biyolojik ve kimyasal ajanların laboratuvar koşulları dışında tayin ve analizinin mümkün hale geldiği görülmektedir. Bu çalışmada, yerinde biyolojik ve kimyasal tayinine yönelik, yüzey plazmon rezonansı algılama ve kızılötesi emilim spektroskopisine dayalı minyatür algılayıcı tasarımları üzerine odaklandık. Kırınım ağı eşlemeli yüzey plazmon rezonansı yüzeyiyle düzlemsel bir fotodiyotu birleştirerek tümleşik refraktometrik algılayıcı geliştirdik. Bu algılayıcı mekanizmasının yüksek tümleştirme yoğunluklu yonga üstü laboratuvar tasarımlarında uygulama alanı bulması öngörülmektedir. Yonga üstü laboratuvar sistemlerinin hasta başı tarama uygulamalarında kullanımına katkı sağlama amacıyla, akıllı telefon tabanlı bir yüzey plazmon rezonansı görüntüleme platformu geliştirdik. Optik veri disklerini kullanarak düşük maliyetli ve hassas kırınım ağı eşlemeli yüzey plazmon rezonansı algılayıcı çipleri ürettik. Sistemin çoklu okuma ve biyomoleküler algılama performansını deneysel olarak ortaya koyduk. Son olarak, cep telefonuyla kızılötesi emilim spektroskopisi ölçümü yapabilen, minyatür bir soğutmasız termal kamera ve özel tasarlanan silikon geçirgenlik kırınım ağını barındıran kompakt bir orta-kızılötesi spektrometresi geliştirdik.

Anahtar sözcükler: Minyatür algılayıcılar, analitik sistemler, yonga üstü laboratuvar aygıtlar, yüzey plazmon rezonansı algılama, kızılötesi emilim spektroskopisi, cep telefonu tabanlı algılama.

Acknowledgement

I would like to express my sincere gratitude to my academic advisor Assist. Prof. Aykutlu Dana for his tremendous support, guidance, encouragement, understanding and patience. It has been a great honor for me to be a part of his research group and complete my Ph.D. degree under his supervision at UNAM-National Nanotechnology Research Center.

I would like to thank Assist. Prof. Ali Kemal Okyay and Assoc. Prof. Mehmet Özgür Oktel for their valuable suggestions and comments throughout this thesis study.

I would like to thank Prof. Adil Denizli and Prof. Hamza Kurt for accepting to be a part of my thesis committee and taking their valuable time to evaluate my dissertation.

I am very much thankful to Assist. Prof. Çağlar Elbüken for his invaluable support and collaboration. I have learnt a lot from him not only in the academic sense but also in terms of personality traits.

I particularly thank Dr. Erol Özgür for being such a great teammate and for his unrequited help.

I owe special thanks to the members of TÜBİTAK BİLGEM Bioelectronics Devices and System Development Group; Dr. Yıldız Uludağ, Güzin Köktürk, Elif Esen and Mehmet Yağmur Gök for their cooperation and contributions.

I feel fortunate to work and discuss with many of my colleagues especially Dr. Burak Türker, Mehmet Çelik, Gamze Torunoğlu, Dr. Sencer Ayas, Ahmet Emin Topal, Hepi Hari Susapto, Dr. Mehmet Kanık, Mustafa Tahsin Güler, Merve Marçalı, Pelin Kübra İşgör, İsmail Bilican, Fahri Emre Öztürk, Assist. Prof. Gökhan Bakan, Nihat Serkan Karayalçın, Mustafa Ürel, Murat Serhatlıoğlu, Dr. Ozan Aktaş, Dr. Ruslan Garifullin, Mehmet Girayhan Say and Ziya Işıksaçan.

I want to express my special thanks to present and former UNAM staff; Mustafa Güler, Semih Yaşar, Hakan Sürel, Berk Berkan Turgut, Halil Volkan Hünerli, Murat Dere, Neşe Özgür, Olcay Ündal, Ayşegül Torun, Duygu Kazancı, Özge Baydar and Dr. Gökçe Çelik,. Indeed, I thankfully acknowledge all UNAM family, especially Prof. Salim Çıracı for pioneering the establishment of such a remarkable research center.

I am grateful to my dear friends Mustafa Kemal İşen, Sinan Gündoğdu, Uğur Karataş, Tuğba İşen, Sercan Çayır, Berkay Ülkü, Durali İpek and Gülşen Gözbulut for their sincere companionship and motivation during the tough times of this work.

I appreciate the moral support of my lifelong friends Osman Pamuk, Mevlüt Akdeniz, Serkan Sonel, Murat Ak, Ali Cevahir and Hüseyin Gökhan Akçay.

I would like to acknowledge The Scientific and Technological Research Council of Turkey, TÜBİTAK, for Ph.D. scholarship and project grants.

And of course, I would like to express my sincere gratitude to my parents and sisters for their endless support and unconditional love. I dedicate this work to my smart nephew Kaan Aydeniz.

Contents

List of Figures

List of Tables

Chapter 1

Introduction

Miniaturization of analytical devices for on-site or point-of-care applications, utilizing lab-on-a-chip technologies, is currently an extremely active field of research [1], [2]for enabling their use in the field, instead of laboratories with a high amount of investment. In particular, SPR based sensing has become a popular method for quantitative analysis and characterization of biomolecular interactions [3]–[5] since it provides label-free and real-time detection of binding events with high sensitivity. Surface plasmon resonance (SPR) sensors rely on the general principle that perturbations in the refractive index of the media interfacing with a metal surface induce an alteration in the resonance of surface plasmons. In terms of biosensing, this alteration corresponds to interaction of analyte molecules with specific molecular probes residing on the surface of the biosensor. The spatiotemporal characteristics of this interaction could be deciphered by real-time tracking of this alteration in terms of either a shift in angle of incidence or resonant wavelength, or a change in the measured intensity at a constant wavelength or angle [6], [7]. Each measurement possesses their own pros and cons in terms of sensitivity and convenience of the measurement, which is also affected by the configuration of optical coupling

to the plasmonic surface [8]; however, angular or spectral interrogation of SPR signals necessitates bulky and expensive equipment such as fine calibrated goniometers [9], [10] or spectrometers [11]. Intensity interrogation of plasmonic resonances, on the other hand, can be performed by utilizing simple and miniature photodetectors [12], [13], or smart phone cameras [14], [15]. This advantage of intensity based SPR measurement could be utilized in order to develop miniature SPR devices, especially when combined with planar grating based SPR substrates.

1.1 Organization of the thesis

In chapter 2, we present an integrated refractometric sensor combining a grating-coupled surface plasmon resonance surface with a planar photodiode. We introduce a brief theoretical background on grating-coupled SPR sensing and estimation of SPR sensitivity. We describe the working principle of integrated sensor design that utilizes plasmon enhanced transmission as a sensitive refractive index sensing mechanism. Planar photodiode was fabricated using a metal induced crystallization procedure. Grating-coupler was integrated with the photodiode substrate using nanoimprint lithography and thin film metallization processes. Surface topography was characterized by atomic force microscopy (AFM). Angular SPR curves were obtained using both numerical calculations and variable angle spectroscopic ellipsometry (VASE). Sensor responses to refractive index changes were measured in real-time during fluid exposures. Further noise reduction was demonstrated using balanced detection.

In chapter 3, we present a surface plasmon resonance imaging (SPRi) platform integrated with a smartphone for on-site high-throughput biodetection. We demonstrate how to develop a compact optical attachment which converts a smartphone into a real-time SPRi instrument together with disposable sensor chips. SPR substrates were obtained by bilayer metal coating on Blu-ray discs.

Flow cells in different structure and geometries were fabricated using laser cutting, 3D printing and polydimethylsiloxane (PDMS) replication molding. Spectral SPR properties were investigated using both simulations and custom-built wavelength interrogation SPR setup. SPR images of Ag/Au bimetallic microspot array were taken using the optical apparatus during flow of glycerol solutions with varying refractive indices. Biodetection performance has been tested through monitoring of bovine serum albumin (BSA) adsorption and selective binding of mouse IgG antibody with immobilized rabbit anti mouse (RAM) IgG antibody.

In chapter 4, we demonstrate infrared absorption spectroscopy on a mobile phone using a miniature uncooled thermal camera. We present dispersive spectrometer configuration for mid-IR spectroscopy that utilizes vanadium oxide microbolometer array technology. A custom transmission diffraction grating was designed using a simulation package based on modified integral method (MIM) and microfabricated out of a silicon wafer through UV optical lithography and inductively coupled plasma (ICP) etching processes. IR transmittance spectrum of a polystyrene film was measured within fingerprint region. Measurement results were compared with ground truth spectra taken by Fourier transform infrared spectroscopy (FTIR) system following further data processing including Fast Fourier Transform (FFT) convolution and blind deconvolution methods.

In chapter 5, we introduce a brief summary of our results and achievements.

Chapter 2

Grating coupler integrated photodiodes for plasmon resonance based sensing

In this chapter, we propose an integrated sensor combining a grating-coupled plasmon resonance surface with a planar photodiode. Plasmon enhanced transmission is employed as a sensitive refractive index (RI) sensing mechanism. Enhanced transmission of light is monitored via the integrated photodiode by tuning the angle of incidence of a collimated beam near the sharp plasmon resonance condition. Slight changes of the effective refractive index (RI) shift the resonance angle, resulting in a change in the photocurrent. Owing to the planar sensing mechanism, the design permits a high areal density of sensing spots. In the design, absence of holes that facilitate resonant transmission of light, allows an easy-to-implement fabrication procedure and relative insensitivity to fabrication errors. Theoretical and experimental results agree well. An equivalent long-term RI noise of 6.3 x 10^{-6} $RIU/\sqrt{Hz}$ is obtained by using an 8 mW He–Ne laser, compared to a shot-noise limited theoretical sensitivity of 5.61 x 10^{-9} $RIU/\sqrt{Hz}$. The device features full benefits of grating-coupled plasmon resonance, such as enhancement of sensitivity for non-zero azimuthal angle of

incidence. Further sensitivity enhancement using balanced detection and optimal plasmon coupling conditions are discussed.

This chapter was published as “Grating coupler integrated photodiodes for plasmon resonance based sensing” by Burak Turker*[1], Hasan Guner*, Sencer Ayas, Okan O. Ekiz, Handan Acar, Mustafa O. Guler and Aykutlu Dana, in *Lab Chip.* 11, 282–287, 2011.

2.1 Introduction

Surface plasmon resonance (SPR) can be exploited as a sensitive refractive index (RI) sensing mechanism and SPR is one of the most common label-free biosensor technologies with a vast variety of applications in biology, food safety, medical diagnostics, agricultural and environmental monitoring [16]. The main concern in the development of SPR is geared toward designing easy to fabricate, cheap and sensitive biosensors with high integration densities. SPR sensors mainly differ in the optical platforms they are based on. Prism couplers [17], [18] result in comparable higher sensitivity values [3] than grating assisted coupling in plasmon resonance excitation. However, the bulky nature of prisms makes them unsuitable for applications in integrated sensing devices. Waveguide couplers [19] employing fibers appear to present the highest degree of miniaturization in SPR sensors, but require expensive high index prisms for the resonant coupling between a surface plasmon and a waveguide mode and suffer from instable sensitivity responses due to deformations in the fiber. Due to their compact size, planarity and stability, grating couplers [20] have benefits in integrated applications. In this work, we present a device that eliminates the traditional far field detection (CCD/CMOS detector) mechanism [21], [22] by using an integrated photodetector design. The device structure is illustrated in Fig. 2.1a and Fig. 2.1b. The detection mechanism works by monitoring the plasmon enhanced

* Corresponding authors.

transmission of light through a thin metal grating that acts as the plasmon resonance sensing surface. Integrating the photo-diode substrate below the grating structure enables the planar geometry and compact integrity of the sensor. As in other SPR sensors, the resonant shifts are only affected by the changes of optical properties within the close vicinity of the surface. Transmission of electromagnetic waves through thin metal films via plasmons has been widely studied in the literature [23]. Plasmon enhanced transmission through sub-wavelength holes [24], [25], nano-hole arrays [26], [27], or periodically corrugated metal surfaces [28] have been investigated theoretically and experimentally [29]. Although plasmon enhancement through nano-hole arrays appears to offer agreeable sensitivity, their realization requires fabrication of holes with high uniformity. Despite the localized nature of plasmon modes in such sub-wavelength aperture arrays and resulting sensitivity to refractive index changes, the overall sensitivity of plasmonic sensors also depends on how sharp the resonances are. Due to fundamental relations between the Fourier components of spatial structure of the surfaces and the SPR, it is difficult to achieve sharp and deep resonances using hole arrays in a simple low-cost fabrication process. In contrast, our approach uses a grating to obtain a plasmonic enhancement of transmission through the silver metallized grating structures. Lack of holes in our design simplifies the fabrication procedure and increases repeatability. Utilizing a bi-harmonic grating topography [30]–[32] rather than a sinusoidal one, observation of higher order resonant coupling is also possible in our devices. The bi-harmonic grating structure allows better excitation of the second order resonance [32]–[34] which also produces an enhancement of light transmission. Such multiple resonances allow SPR detection at a fixed angle of incidence (AOI) for multiple different wavelengths.

2.2 Theoretical aspects of grating coupling to the plasmon mode and estimation of SPR sensitivity

The momentum mismatch between the in-plane wave vector of impinging photons and the wave vector component of the excited surface plasmons disables a natural momentum coupling at planar surfaces. On a smooth planar interface of a metal and a dielectric, the surface plasmon polariton (SPP) wave vector, k_{SPP}, is found to be always greater than the wave vector of incident light in air, k_0, as given by

$$k_{SPP} = \frac{\omega}{c}\sqrt{\frac{\varepsilon_m \varepsilon_d}{\varepsilon_m + \varepsilon_d}} \geq k_0 = \frac{\omega}{c}\sqrt{\varepsilon_d} \tag{2.1}$$

where ε_m is the permittivity of the metal layer and ε_d is that of the dielectric layer (fluid). One of the techniques for satisfying this energy and momentum match condition is to employ grating schemes. The presence of a metal planar surface that is patterned with a shallow grating of grooves with some periodicity modifies equation (2.1) as follows

$$k_{SPP} = m\frac{2\pi}{\Lambda} + k_{0,InPlane} \tag{2.2}$$

where m is an integer denoting the diffraction order, $k_{0,InPlane} = k_0 \sin(\Theta_R)$is the in-plane vector of the incident light and Λ is the grating period. And thus a plane wave approaching the surface can resonantly couple to the plasmonic excitation at a particular angle of incidence defined by

$$\Theta_R = \sin^{-1}\left[\left(Re\left\{\sqrt{\frac{\varepsilon_m \varepsilon_d}{\varepsilon_m + \varepsilon_d}}\right\}\right) - \frac{m\lambda}{\sqrt{\varepsilon_d}\Lambda}\right] \tag{2.3}$$

If the measurement is performed inside a fluidic channel with a transparent planar top window, the incidence angle Θ_i inside the fluidic chamber will be different than that in air, and must be corrected according to Snell's law.

When an organic thin film is applied to the surface the change in the plasmon wave vector [35] can be approximated by

$$\delta k_{SPP} \cong \frac{k_{SPP}^3}{k_0^2 n_d^3}[1 - exp(-2\gamma_d h)]\Delta n \tag{2.4}$$

where $\gamma_d = ik_0\varepsilon_d/\sqrt{\varepsilon_m + \varepsilon_d}$ and the plasmon mode field penetration depth into the dielectric is $L_{PD} = 1/Re\{\gamma_d\}$. Also, Δn is the refractive index difference of the fluid and the organic thin film and h is the thickness of the organic thin film. In the presence of an organic film thickness $h \ll L_{PD}$, the resonance angle shift can be approximated through equations (2.2), (2.3) and (2.4) as

$$\delta\Theta_R = \frac{k_{SPP}^3 2\Delta n}{k_0^3 n_d^3 L_{PD}\cos(\Theta_R)} h \tag{2.5}$$

Overall sensitivity depends on the interrogation method (intensity, wavelength or angular). The sharpness of the resonance peak also is a factor in determination of the sensitivity, most evident in the intensity measurement schemes. When a thin metal layer (~ 30 to 100 nm) is used in the grating coupler, whenever the plasmon is excited, it is partially re-radiated (transmitted) into the substrate (Fig. 2.1c). This plasmon enhanced transmission takes place for higher order resonant coupling or for non-zero azimuth excitation as well. Therefore, the transmission type device features the full benefits of grating coupled plasmon resonance. Sensitivity optimization of transmission type devices are the same as reflection type grating coupled plasmon resonant devices. However, metal thickness has to be optimized as well. Near a resonance condition, the transmitted intensity can be approximated by

$$T(\Theta_i, \Theta_R) \cong \frac{T_0}{1+4(\Theta_i-\Theta_R)^2/\Delta\Theta^2} \quad (2.6)$$

where Θ_i is the angle of incidence, Θ_R is the resonance angle and $\Delta\Theta$ is the full-width at half-maximum (FWHM) of the resonance (Fig. 2.1d). In the intensity interrogation scheme, the illumination is incident at a fixed angle Θ_i and transmitted intensity is monitored. Maximum SPR sensitivity is achieved when $|\delta T/\delta\Theta_R| \sim 2T_0/\Delta\Theta$, which takes place when $\Theta_i \sim \Theta_R \pm \Delta\Theta/4$. Theoretical refractive index sensitivities of the first and second order resonances are 50 ^{o}/RIU and 81 ^{o}/RIU for 740 nm period grating in $n_d = 1.33$ fluid with an excitation wavelength of 632.8 nm. Optimal grating depth is 30 nm and calculations assume 45 nm silver film. The FWHM of both the first and second order resonances are $\Delta\Theta \sim 2^o$ with a peak transmission of $T_0 = 0.3114$ for the first order and $T_0 = 0.167$ for the second order. Under these optimal conditions, assuming a 1 mW illumination and 0.4 A W^{-1} responsivity of the silicon readout photodiode, the first order resonance yields a current sensitivity of 6.2 mA/RIU. In this configuration, the photodiode current is calculated to be 62.3 mA and the corresponding shot noise current is 4.46 $pA/\sqrt{Hz}$. Therefore, shot noise limited minimum detectable refractive index is calculated to be 7.19 x 10^{-10} $RIU/\sqrt{Hz}$. This sensitivity level would require the measurement of current to 1 part in 1.4 x 10^7. If the precision of measurement is limited by electronics to 1 part in 65536 (16 Bits), the minimum detectable refractive index is calculated to be 1.53 x 10^{-7} $RIU/\sqrt{Hz}$. If the second order resonance is used, the reduction in the peak transmission compensates for the greater angular sensitivity (81 Deg/RIU for the second order compared to 50 Deg/RIU for the first order), and a similar refractive index resolution is obtained.

2.3 Experimental

The sensor assembly, photographed in Fig. 2.1a and schematically illustrated in Fig. 2.1b, has a sandwich structure of three integrated layers. On top, there exists a polymethyl methacrylate (PMMA) cover forming the flow channel. A photodiode substructure lying at the bottom serves as a detector and in between there is the patterned and metallized transparent polymer, i.e. the grating structure, to function as the surface plasmon (SP) coupler.

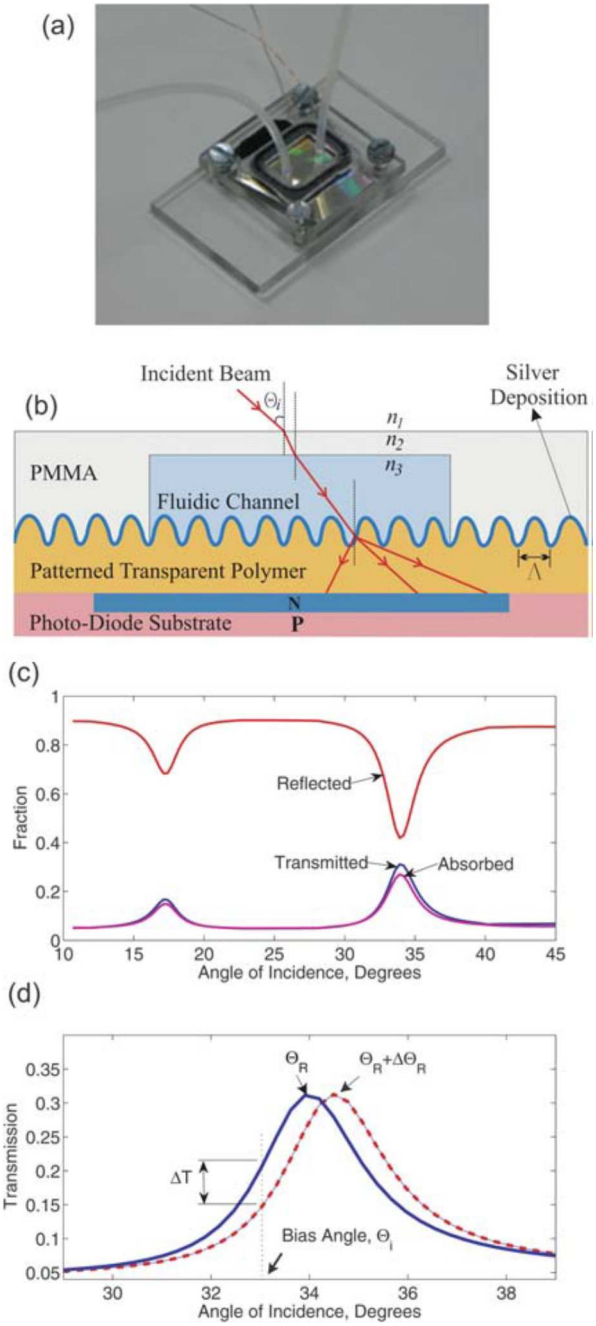

Figure 2.1: (a) Photograph of the sensor device with a PMMA fluidic chamber and in/outlet tubing. (b) Cross-sectional schematic view of the device structure. (c) Simulation results of the reflection, transmission and absorption data for TM polarization in the case of a 30 nm deep sinusoidal grating, deposited with a 45 nm thick Ag layer and illuminated by a 632.8 nm light source. The working medium is water with $n_d = 1.33$. (d) The operational principle of the device is schematically shown. The illumination is kept at a fixed angle Θ_i and a small perturbation ($\delta\Theta_R$) of the resonance condition (Θ_R) results in a change (δT) in the transmitted intensity.

2.3.1 Photodiode substrate fabrication

In order to demonstrate that the device can be realized on standard silicon substrates with low-cost and widely available manufacturing equipment, the photodiode was fabricated using a metal induced crystallization procedure as described previously [36]. First an amorphous silicon layer is deposited (in bare brown color) on to an n-type silicon wafer (in purple) by using plasma enhanced chemical vapor deposition (Fig. 2.2a). An aluminum layer (with a mass thickness of 50 nm) was deposited on-top using thermal evaporation and it was then annealed (in a N_2 atmosphere at 500 ^oC for 30 min) for partial crystallization and p-type doping of the n-type Si-wafer substrate (Fig. 2.2a). The aluminum residue on the surface, i.e. the unreacted aluminum after the partial induced crystallization (due to thermal annealing), was cleaned by using hydrofluoric acid (HF) rinse (Fig. 2.2b). Then, an additional aluminum layer was deposited by thermal evaporation and the deposited layer was lithographically patterned for making contact pads for the p-type (aluminum, top) region (Fig. 2.2c). The contact pad for the n-type region was made by deposition of a gold–palladium layer on the backside of the wafer (Fig. 2.2c). The device has also been fabricated using commercial photodiodes and it was observed to produce a similar performance.

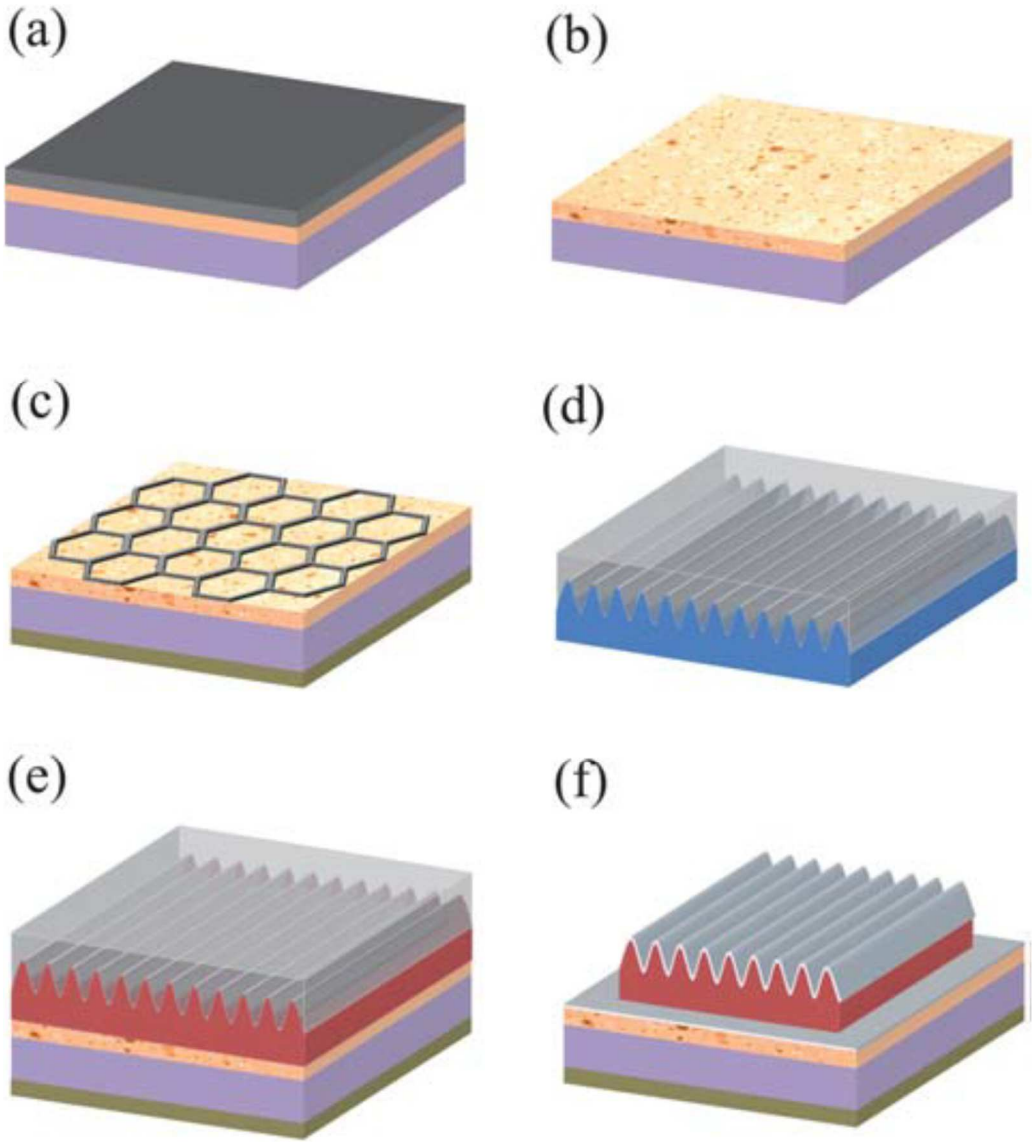

Figure 2.2: Fabrication steps of a grating coupler-integrated photodiode ((a)–(f)). (a) n-type Si wafer, amorphous Si, aluminum (from bottom to top). (b) Amorphous Si is aluminum doped during thermal curing. (c) Contact pads on top-side are patterned by lithography of an additionally deposited Al layer. Photodiode substrate is completed by the deposition of gold–palladium at the bottom-side to form the contact pads. (d) Grating profile is replicated from a surface modified DVD disc. PDMS is poured on the master mold and cured at 70 ^{o}C for 5 h. Cured PDMS is peeled off from the master mold and used as elastomeric stamp. (e) Photoresist polymer is spin-coated on the photodiode substrate. Elastomeric stamp is released gently on the polymer film and hard-baked. Stamp is mechanically removed from the sample. (f) Contact mask is defined by the optical lithography. Thin Ag film is thermally evaporated to be used for plasmonic coupling.

2.3.2 Nano-imprinted mold fabrication

Gratings were replicated using the elastomeric molding technique by nano-imprinting [37], [38]. Previously, we have shown that modified optical disc surface profiles can be used to excite sharp and well defined plasmon resonances [39]. Various tuned grating profiles were studied experimentally and theoretically [40]. For $n_d \sim 1.33$, the optimum grating structure has a groove depth of 30 nm with a tuned Ag film thickness of 45 nm. The optimal topography and metal thickness produce the desired sharp resonance curves with high transmission. Thicker films reduce the transmission of stray light at the expense of reduced transmission of the signal. Gratings derived from Digital Video Disc (DVD) surfaces had a similar topographic corrugation (45 nm) and were used as the master mold. Polydimethylsiloxane (PDMS) (Slygard 184, Dow Corning) was poured on the substrates and cured at 70 ^{o}C for 5 h (Fig. 2.2d). After curing, PDMS was peeled off from the master mold and used as an elastomeric stamp. A photoresist (AZ5214, AZ Electronic Materials) diluted 1 : 3 by a photoresist thinner (AZ1500, AZ Electronic Materials) was spin-coated at 8000 rpm in order to form the grating material. Elastomeric stamp was then released softly on the thinned photoresist film and hard baked on a hotplate at 120 ^{o}C for about 5 min. Finally, the stamp was mechanically removed from the sample (Fig. 2.2e). Metallization is done by thermally evaporation of silver onto the imprinted grating (Fig. 2.2f). The described procedure does not require external pressure to be applied to the PDMS stamp and results in uniform and distortion free gratings over large areas (greater than 10 cm^2).

2.3.3 Measurements

Measurements were performed on an optical table with various He–Ne laser sources (2 mW and 8 mW nominal power) and a 650 nm laser diode (5 mW nominal power) was used to excite surface plasmon polaritons. Both TE and TM polarizations were measured, plasmon coupling is seen to occur for TM mode only. The grating direction is kept perpendicular to the plane of incidence and zero azimuthal angle was chosen. The angle of incidence (AOI) was stepped in the angular range of -50 and +50 degrees. In order to test the refractive index sensitivity of the device, distilled water (nominal refractive index 1.33) and a 5% NaCl solution (nominal refractive index 1.342) were used. Liquid samples were streamed into the fluidic channel utilizing gravity. Photodiode outputs were monitored using precision current meters (Keithley 2400).

2.4 Results and discussion

2.4.1 Grating profiles

Grating surfaces were characterized by using atomic force microscopy (AFM) (Fig. 2.3a). In comparison to a uniform profile, a bi-harmonic surface profile enhances the second order coupling to the plasmon mode. Both resonances were observed in the reflection (in Fig. 2.3b) and transmission mode measurements (Fig. 2.3c). Plasmonic properties of silver coated gratings were characterized by measuring the reflection spectra using variable angle spectroscopic ellipsometry (using a J. A. Woollam, VASE system).

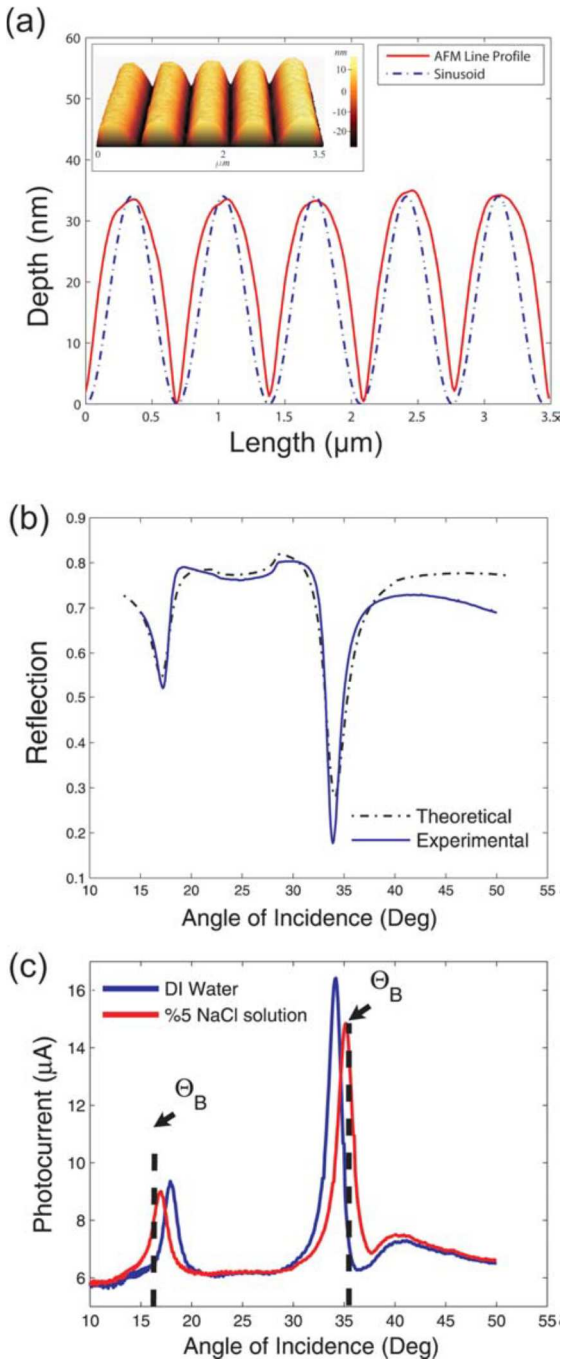

Figure 2.3: (a) AFM line profile of the grating structure with a depth of 35 nm is depicted compared to a sinusoidal grating profile. Inset figure illustrates AFM topography of the corresponding grating structure with a groove depth of 35 nm and 45 nm thick silver coating. (b) Reflection behavior of the grating structure is depicted in water medium under incidence of a 632.8 nm wavelength light source. Solid lines show the reflection measurement results whereas the dashed lines show theoretical results. (c) Measured photocurrent response of the integrated sensor as a function of the angle of incidence for water and NaCl solution. Bias angles used in the time-resolved measurements are shown by arrows.

2.4.2 Plasmon resonance characteristics and sensitivity

We calculate the resonance angles for 632.8 nm excitation on a $\Lambda = 740\ nm$ grating surface, using silver as the metal layer. The first and second order resonances are calculated to occur at $\Theta_R = 33.9^o$ and 17.4^o for $n_d = 1.33$ (after correction for refraction at the air/cover interface). Theoretical resonance angles are shifted to 34.8^o and 16.6^o for $n_d = 1.342$ (representing NaCl solution). Experimentally measured resonance angles closely match the theoretical values. In DI water, the first and second order resonances are measured to occur at $\Theta_R = 34.1^o$ and 17.9^o, while the angles shift to $\Theta_R = 35.2^o$ and 16.9^o for NaCl solution. Both resonances have FWHM of $\Delta\Theta \sim 1.5^o$. Contrary to theoretical calculations, the angular sensitivities of the resonance are observed to be 91 Deg/RIU and 83 Deg/RIU. The discrepancy may be due to systemic measurement errors of the resonance angles in our measurement setup. In time resolved measurements, DI water and NaCl solution were streamed through the fluidic channel and photocurrents were monitored (Fig. 2.4a and 2.4b).

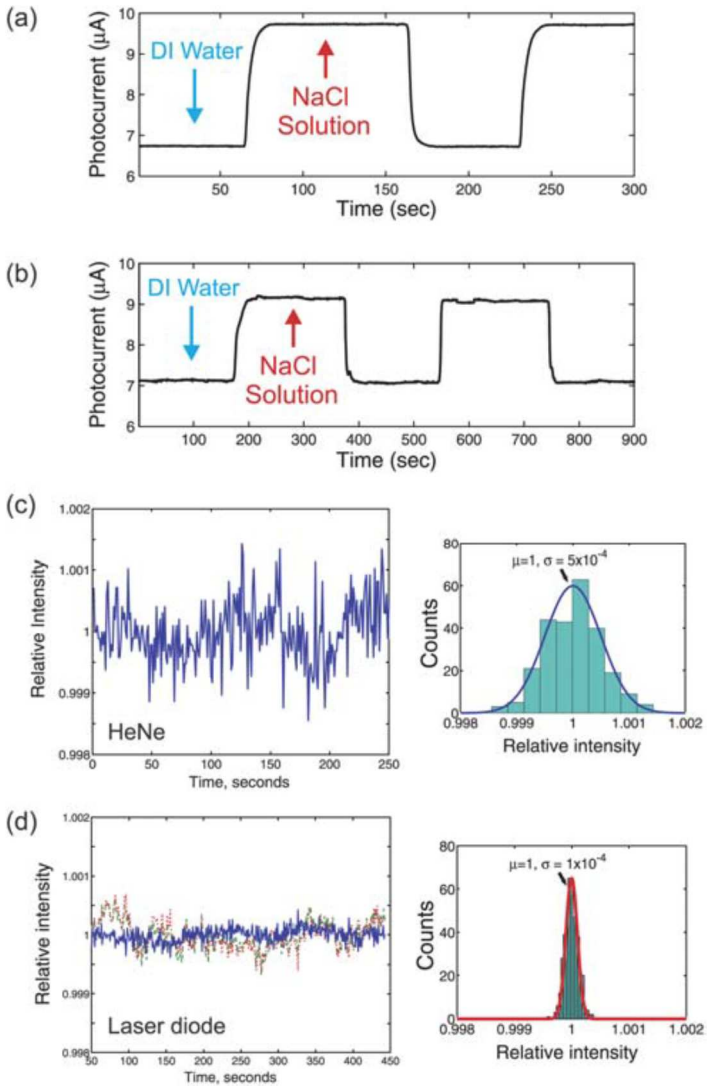

Figure 2.4: Sensor responses to fluid exposures: (a) around the 2nd order resonance peak biased at 17.1^o and (b) around 1st order resonance peak biased at 35.6^o respectively. A 632.8 nm HeNe laser source is used, resulting in an equivalent refractive index noise of 6.3 x 10^{-6} $RIU/\sqrt{Hz}$. (c) Stability of the measurement set-up using a 2 mW HeNe source and (d) using a power stabilized 650 nm laser diode. Further noise reduction is demonstrated using balanced detection. In (d) a reference photodiode monitors the light intensity at the source while the device is biased near the first order resonance. Normalized intensities for the reference diode (dotted) and SPR diode (dashed) are shown as well as the ratio of the two (solid). In the balanced measurement, the SPR intensity signal can be measured with a $0.01\ \%/\sqrt{Hz}$ relative intensity noise. Resulting detection noise floor is 1.2 x 10^{-6} $RIU/\sqrt{Hz}$. Histograms of current readings are shown with corresponding Gaussian curve fits.

The bias angles are chosen such that an increase of the refractive index causes an increase of the photocurrent ($\Theta_i = 35.6^o$ and 17.1^o, See Fig. 2.3c). The current sensitivity at the highest slope of the transmission curve is experimentally determined to be $\delta i/\delta\Theta_R = 7.37\ \mu A/Deg$ for the first order and $\delta i/\delta\Theta_R = 2.92\ \mu A/Deg$ for the second order. The resulting overall sensitivities can be then calculated $\delta i/\delta n = 6.11\ \times 10^{-4}\ A/RIU$ for the first order and $\delta i/\delta n = 2.42\ \times 10^{-4}\ A/RIU$ for the second order. The main reason for the observed reduced value of $\delta i/\delta n$ (compared to $\delta i/\delta n = 6.2\ \times 10^{-3}\ A/RIU$ for the optimal design with 1 mW laser power) is that the thickness of the silver layer is about 130 nm (greater than the optimal value of 45 nm). For the present device and assuming a shot-noise limited measurement, the minimum detectable refractive index change is estimated as 5.61 x 10^{-9} $RIU/\sqrt{Hz}$. However, due to laser source dominated noise during measurements (Fig. 2.4c), this value was determined as 6.3 x 10^{-6} $RIU/\sqrt{Hz}$. The measured photocurrent noise level near DC is around 1.7 $nA/\sqrt{Hz}$ as opposed to a theoretical shot noise level of 1.8 $pA/\sqrt{Hz}$. Using a laser diode and an external reference photodiode, the transmitted intensity can be measured to an accuracy of 1 part in 10^4, yielding a sensitivity of about 1.2 x 10^{-6} $RIU/\sqrt{Hz}$ (Fig. 2.4d).

2.4.3 Discussion

We demonstrated detection of changes in the RI of the streamed solutions (DI water and 5% NaCl solution) with reversible, repeatable and stable sensor response, yielding an equivalent RI noise of 6.3 x 10^{-6} $RIU/\sqrt{Hz}$ (limited by the laser intensity noise and instrumental drifts). For the present device, optimization of the coupling condition may further enhance the sensitivity. It is well known that as the coupling angle Θ_R approaches grazing angles, the angular sensitivity increases [8]. This fact is also predicted in equation (2.5), as the angular sensitivity is dependent on Θ_R, i.e. $\delta\Theta_R/\delta n_d \propto 1/\cos(\Theta_R)$. The sensitivity can be further enhanced by about an order of magnitude, by choosing a different grating period

or excitation wavelength, so that $\cos(\Theta_R) \sim 0.1$. Also, recently Romanato et al.[41], [42] reported that azimuthal rotation of the grating results in a larger resonance angle shift (up to 800 Deg/RIU compared to 50~100 Deg/RIU for our present configuration). For optimal azimuthal excitations, a sensitivity improvement of more than an order of magnitude should be achievable in our device, compared to the same grating excited with zero azimuth angle. In such a case, the sensitivity is expected to be $\sim 10^{-7} RIU/\sqrt{Hz}$ for a relative readout accuracy of 10^{-4}. The shot noise limited detection limit also benefits from such an improvement and can be on the order of $1 \times 10^{-10} RIU/\sqrt{Hz}$ using 1 mW illumination. Although systemic errors lead to slight discrepancies between theory and experiment, the sensitivity is estimated to be on the correct order. The device we present here is particularly appropriate for array detection and balanced detection. For example, by integrating the grating coupler onto an array detector (such as a CCD), multiple sensing spots can be monitored simultaneously. Using differential functionalization, balanced detection can be done within the same chip. Such an in situ balanced detection potentially eliminates temperature related drifts and renders the device insensitive to refractive index fluctuations of the working fluid. Another way of performing array sensing is by using focused illumination. Such area-selective illumination allows a single large-area photodiode to be used to detect the resonance signal from a multitude of individually functionalized sensing spots. The well-known relation between the focal spot size (D) and beam divergence (θ_d) in diffraction limited focusing ($D = 2\lambda/\pi n_d \sin(\theta_d)$) determines the minimum allowed beam divergence for a given spot size. If a focused beam is used, an effective broadening of the resonance peak is observed, which reduces the sensitivity. For a divergence angle of about 1 degree, a spot diameter of about $20\ \mu m$ is achievable with 632.8 nm light in water. Such an angular dispersion is seen to degrade the sensitivity only by about a factor of two.

2.5 Conclusion

Using a straightforward, easy-to-implement fabrication procedure, we demonstrated the possibility of achieving very promising sensitivity and sensor responses through integration of the grating coupled plasmon detection mechanism with the optical sensor. Our approach yielded a low cost, SPR sensor which could offer a high level of miniaturization. The device features the full benefits of grating coupled plasmon resonance, with room for sensitivity enhancements to levels comparable with prism coupled sensing. The detection scheme can find applications in integrated lab-on-chip designs where label free detection is desirable.

Chapter 3

A smartphone based surface plasmon resonance imaging (SPRi) platform for on-site biodetection

In this chapter, we present our studies on the demonstration of a surface plasmon resonance imaging platform integrated with a smartphone to be used in the field with high-throughput biodetection. Inexpensive and disposable SPR substrates are produced by metal coating of commercial Blu-ray discs. A compact imaging apparatus is fabricated using a 3D printer which allows taking SPR measurements from more than 20.000 individual pixels. Real-time bulk refractive index change measurements yield noise equivalent refractive index changes as low as 4.12×10^{-5} RIU which is comparable with the detection performance of commercial instruments. As a demonstration of a biological assay, we have shown capture of mouse IgG antibodies by immobilized layer of rabbit anti-mouse (RAM) IgG antibody with nanomolar level limit of detection. Our approach in miniaturization of SPR biosensing in a cost-effective manner could enable realization of portable SPR measurement systems and kits for point-of-care applications.

This chapter was accepted for publication and appeared online as “A smartphone based surface plasmon resonance imaging (SPRi) platform for on-site biodetection” by Hasan Guner, Erol Ozgur, Guzin Kokturk, Mehmet Celik, Elif Esen, Ahmet E. Topal, Sencer Ayas, Yildiz Uludag, Caglar Elbuken, and Aykutlu Dana, in *Sensors and Actuators B: Chemical* 239, 571-577, 2017.

3.1 Introduction

The wide use of mobile phones all across the world created significant opportunities for healthcare applications using mobile devices. Improvement of healthcare services requires democratization of the services with higher quality and lower cost. Early diagnosis, close monitoring, patient comfort are some of the concerns that healthcare providers are striving to improve on. The development of lab-on-a-chip platforms in the last two decades brought several examples of novel platforms that can be used for rapid diagnosis of widespread diseases. Portability, short turn-around-time, cost-efficiency and connectivity are some of the critical assets that successful devices should possess. The advancements in such areas enabled the use of lab-on-a-chip systems as on-site or point-of-care systems not only for remote or resource-limited settings, but also for home-monitoring of elderly population at developed countries.

One of the main bottlenecks in transforming the lab-on-a-chip systems into point-of-care diagnostic devices is the requirement to miniaturize and combine several off-chip components. The marriage of the lab-on-a-chip systems with mobile phones was the tipping point that yielded a plethora of integrated screening and diagnostic devices. Mobile phones provide powerful CPUs, touch screen displays, advanced connectivity features as well as high pixel-count, sensitive cameras and integrated light sources. Therefore, the use of mobile phones for applications requiring optical detection is an interesting and rapidly developing field of research. For instance, immunodiagnostic assays, lateral flow assays,

microscopic imaging, flow cytometry, colorimetric detection, photonic crystal and surface plasmon resonance (SPR) based biosensing have been demonstrated using mobile phone platforms [14], [15], [43]–[52]. In this study, to the best of our knowledge we present the first surface plasmon resonance imaging on a smartphone.

SPR biosensing is a popular method for quantitative analysis and characterization of biomolecular interactions [3]–[5]. SPR provides label-free and real-time detection of binding events with high sensitivity Surface plasmons are electromagnetic waves propagating along and evanescently decaying away from the metal/dielectric interface. This field confinement around the boundary makes plasmon resonance coupling condition extremely sensitive to the local refractive index changes caused by specific adsorption of target analytes onto the molecular probes residing on the metal surface. Recently, some studies have demonstrated SPR sensing using smartphone. Preechaburana et. al. reported angle-resolved SPR chemical detection using an SPR coupler attached on the smartphone screen utilizing the illumination from the screen [50]. In order to develop a more practical system, Liu et. al. [14] and Bremer et. al. [51] showed the use of optical fibers for SPR detection on cell phones. Both of these systems used the back-side LED and camera of the cell phone as the light source and the sensor, respectively. Roche et. al. demonstrated localized SPR sensing on cell phone with increased sensitivity using gold nanoparticles and nanorods [15]. Dutta et. al. reported localized SPR (LSPR) sensing on cell phone for biomolecular detection and measuring size variation of metal nanoparticles [52]. All of these studies, demonstrate single-spot or 1D spatially resolved SPR sensing, which limits their applicability for high-throughput and multiplexed detection. In this article, we demonstrate SPR imaging or 2D SPR sensing on a cell phone, unveiling the potential of multi-analyte detection as well as implementation of array-based advanced biochemical analysis using a low-cost, integrated platform.

SPR imaging is superior to single-spot SPR since it can be used for detection of multiple analytes in a single sample for panel assays. This leads to significant benefits in terms of cost and measurement time. Similarly, the multiple sensing points on the sensor can be used for detection of the analyte at several sample dilutions which is critical for serial dilution assays. Also, image-based bioanalytical detection helps the operator to view the results at once and interpret them more easily. Additionally, image-based 2D sensing can provide replicated measurements on the same sensor chip together with controls that leads to higher reliability, precision and on-chip self-calibration. On-chip control and self-calibration are especially critical for point-of-care sensing applications that suffer from high error rates due to varying operating conditions and the wide range of user levels. We believe the demonstration of such advanced biochemical techniques using mobile phones and cost-effective sensors will lead to a paradigm shift in the global healthcare market. Implementation of advanced detection applications on continuously improving feature-rich mobile phones will pave the way towards highly sensitive diagnosis tools reaching to the people from all socio-economic levels.

Here, we present surface plasmon resonance imaging on a smartphone. We have developed very low-cost grating coupled SPR sensor chips using off-the-shelf optical storage discs. Additionally, we designed a compact optical system, using a 3D-printed apparatus that hosts the LED source, collimator, bandpass filter, linear polarizer, beamsplitter plate and an external imaging lens which can be easily attached to the smartphone. We employed a silver-gold bilayer structure coated on the periodic corrugations of Blu-ray discs in order to perform plasmon resonance imaging at the central region of visible spectrum (λ_r~500 nm) under normal incidence illumination in aqueous environment. This allowed the optimal use of the CMOS sensor of the smartphone while maintaining high sensitivity, chemical stability and biological affinity [53]–[56]. A microfluidic channel is placed on the bi-metallic layer for controlled plumbing of the liquids. The use of Blu-ray discs and standard metal deposition techniques together with the low-cost

microfluidic channel resulted in significant cost-reduction which can allow the system to be used for applications requiring disposable SPR sensors.

3.2 Materials and Methods

3.2.1 Smartphone attachment for surface plasmon resonance imaging

An optical attachment was developed which converts smartphone into a real-time surface plasmon resonance imaging platform based on intensity interrogation mechanism. A Samsung I8552 Galaxy Win was used as the smartphone. The prototype accessory was fabricated out of polylactic acid (PLA) filament using a 3D printer (MakerBot Replicator 2). Optical configuration of the imaging platform is schematically illustrated in Fig. 3.1a. Light emitting from a 520 nm LED source is coupled to a multimode fiber optic cable (acting as a spatial filter) and collimated by a fiber optic collimator. A bandpass interference filter (λ_c=520 nm, $\Delta\lambda_{FWHM}$=10 nm) is used to narrow the spectral bandwidth of illumination. Collimated beam of light becomes transverse magnetic (TM) polarized passing through a linear polarizing filter sheet and is directed onto the sensor surface at normal incidence by reflecting from a beamsplitter plate. Light reflecting off the sensor surface passes through the beamsplitter plate and is focused on the smartphone's camera sensor by an external plastic imaging lens (focal length=8 mm). Imaging spot covers approximately 160 pixels in diameter, although the camera is capable of video recording at 720 x 480 pixels resolution. Imaging resolution is calculated as 12 μm/pixel. Only green channel of RGB image is analyzed since it has the highest spectral responsivity at the operation wavelength. The attachment measures 143 x 75 x 44 mm^3 and weighs 215 grams including 2 AAA batteries (Fig. 3.1b).

An Android application software was developed to analyze image data, report intensity changes and estimate analyte concentration in the field use (Fig. 3.1c). When the app is initiated, zoomed in view of the imaging spot is displayed

continuously at the background. First, region of interests (ROI) on the sensor surface are defined by tapping menu button and entering ROI parameters in the settings menu. To estimate analyte concentrations from intensity changes, predetermined calibration line parameters are set in slope, intercept and unit fields. Time averaging feature can be activated by entering the number of consecutive frames to be averaged. “Reference”, “Dark” and “Baseline” buttons are used to take and store reference, dark and baseline intensity values, respectively, as described in subsection 3.2.3. Averaged intensity changes and estimated analyte concentrations for each ROI segment are displayed separately on the right side of the screen when the “Start recording” box is checked. Unchecking the “Start recording” item stops recording and saves measurement data in a text file. Screen captures from application software are presented in Fig. 3.2.

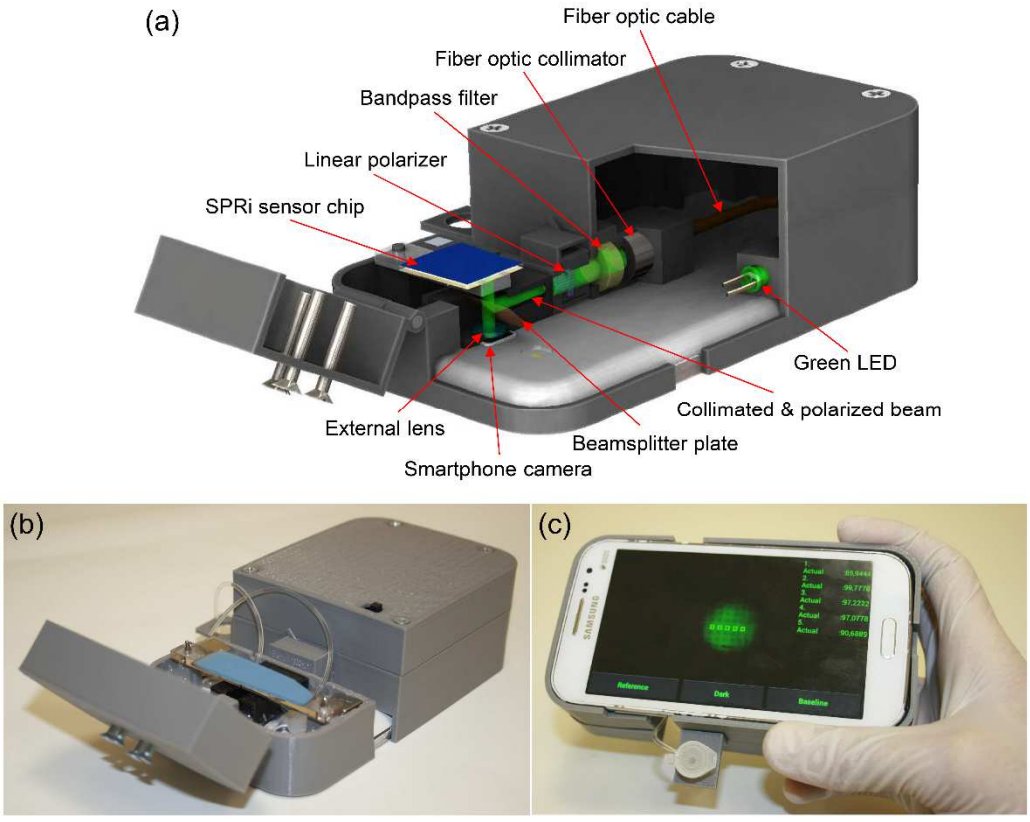

Figure 3.1: Surface plasmon resonance imaging platform integrated with a smartphone. (a) Schematic illustration and (b) photograph of the imaging apparatus. (c) Custom developed smartphone application for real-time and on-site monitoring of multiple sensing spots.

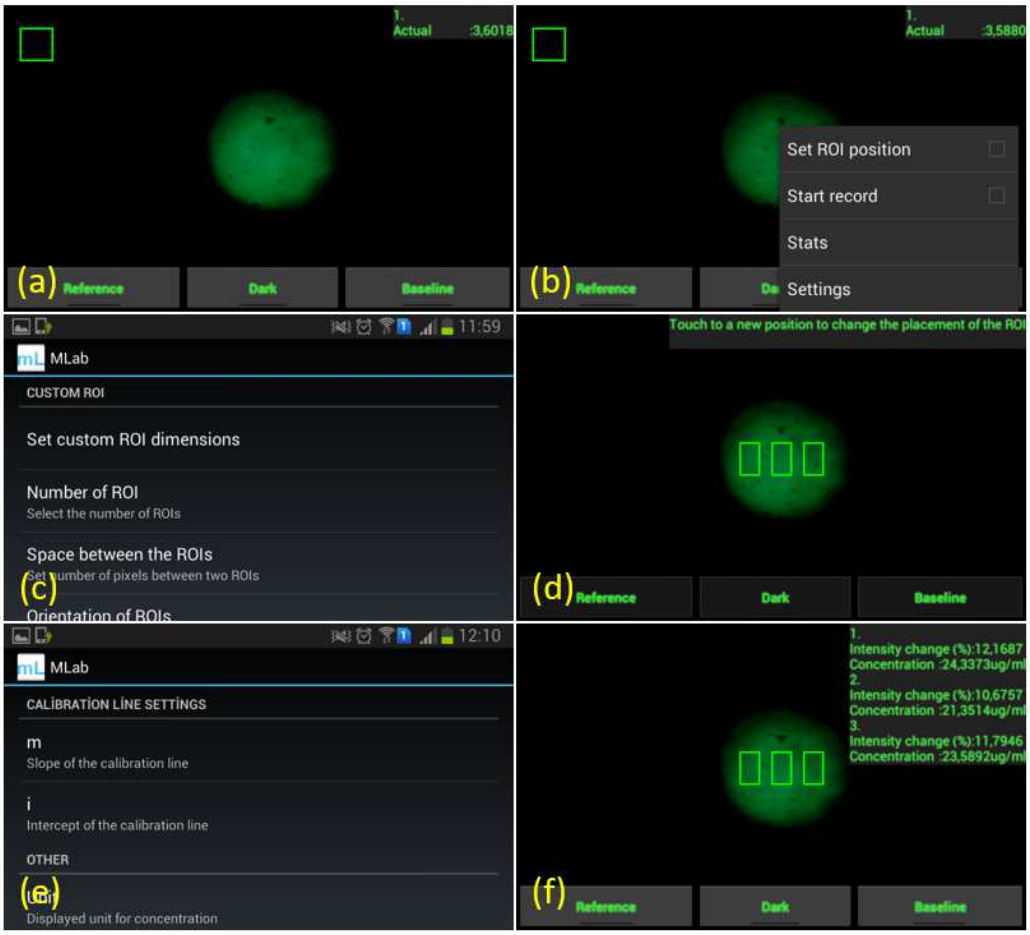

Figure 3.2: Smartphone application software. (a) When the app is started, zoomed in view of the imaging spot is displayed at the background overlaid by “Button menu” at the bottom, and “Report table” at the top right corner. (b) “Control menu” pops up at the bottom right corner when the menu button of the smartphone is tapped. (c) Region of interest (ROI) parameters are defined in the “Settings menu”. (d) ROI frames are overlaid on the imaging spot. (e) Other input values like calibration line parameters and number of averaging frames are entered in the “Settings menu”. (f) Following the measurement of reference, dark and baseline intensities by using the buttons in the “Buttons menu”, actual measurement is initiated by checking the “Start record” item in the “Control menu”, and averaged intensity change and estimated analyte concentrations for each ROI are updated separately in the “Report table”. Measurement data is automatically saved in a text file when the recording is stopped by unchecking the “Start record” item.

3.2.2 Design and fabrication of SPRi sensor chips

Optical storage discs can be exploited as grating coupled surface plasmon resonance sensors by metal coating, thanks to the periodic corrugations (Fig. 3.3) [39], [57].

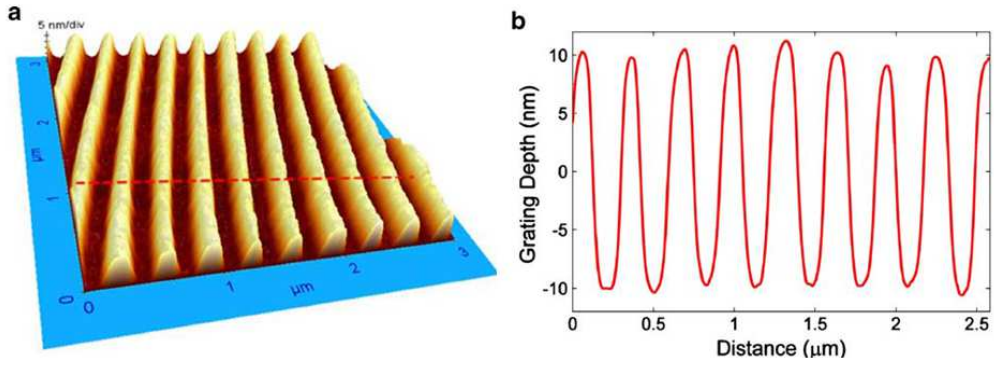

Figure 3.3: (a) AFM micrograph of Blu-ray disc surface and (b) line profile.

Depending on the disc type and refractive index of the surrounding medium, surface plasmons can be excited at wavelengths ranging from ultraviolet to near infrared spectral regions. SPR substrates produced from Blu-ray discs (BD) (grating period Λ=320 nm, grating depth d=20 nm) exhibit plasmon resonances within the visible spectrum when illuminated at normal incidence in aqueous medium, as indicated by the reflectance spectra calculations (Fig. 3.4).

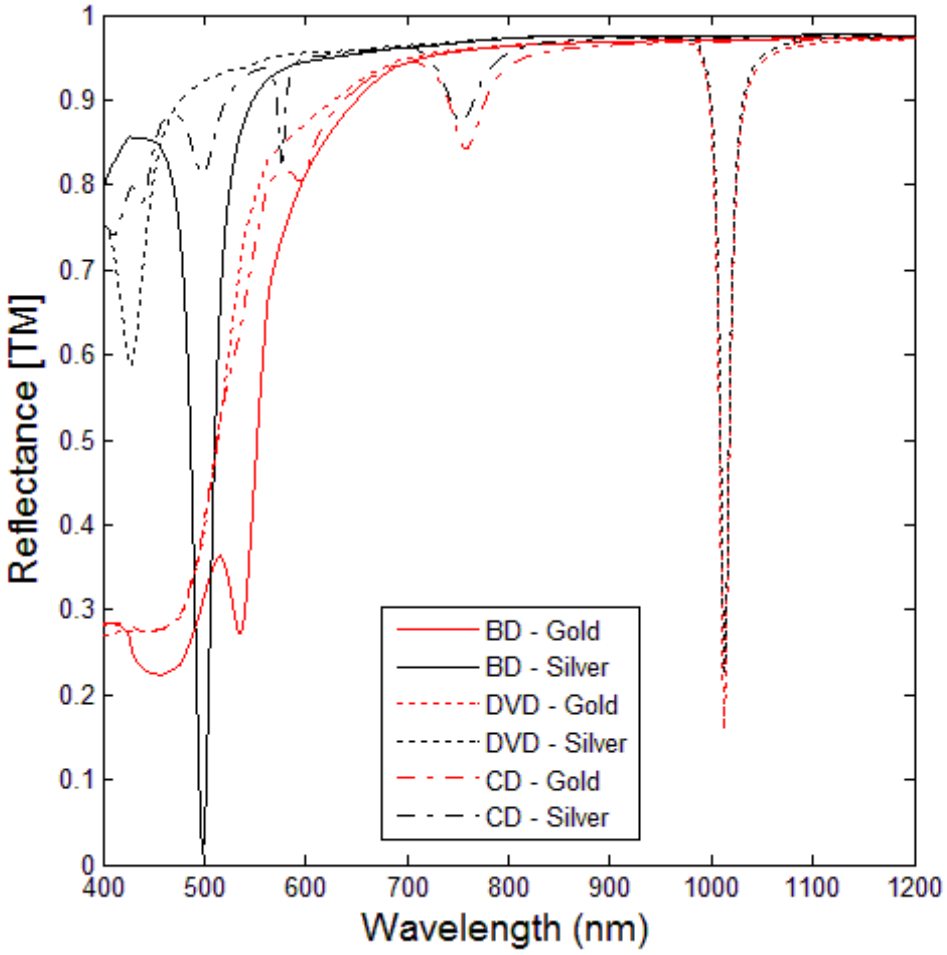

Figure 3.4: Calculated reflectance spectra of various types of metallized optical discs under normal incidence of illumination in water medium. Grating periods of Blu-ray Disc (BD), Digital Versatile Disc (DVD) and Compact Disc (CD) are 320 nm, 740 nm and 1.6 μm, respectively.

Numerical calculations are performed using a commercial software which employs modified integral method (MIM) [40]. PCGrate allows calculation of diffraction efficiencies of multilayered 1-D gratings. Calculation mode should be switched from normal to resonance mode for SPR coupler simulations. Polarization of the incident beam is set as non-polarized in order to examine the reflectance spectra for both transverse electric (TE) and transverse magnetic (TM) polarized illuminations. Surface profile of the grating on BD is defined as sine-trapezoidal using built-in geometrical tools. Complex refractive indices of gold and silver are extrapolated from previously taken experimental data [58].

According to the simulation results, silver coated BD exhibits sharp plasmon resonance around 500 nm wavelength, whereas gold coated BD does not display surface plasmon resonant behavior at normal incidence of excitation due to its intrinsic absorption characteristics at this portion of the spectrum. However, gold has superior properties over silver in terms of chemical stability and adequacy for further surface functionalization chemistry for biosensing applications. In order to overcome this dichotomy, we came up with a hybrid solution in which thick (>80 nm) silver coating at the bottom acts as a plasmon excitation layer and thin (<10 nm) gold film on top functions as a surface for the subsequent surface modification, as well as extending the shelf life of the sensor chip. The thicknesses of Ag and Au layers are optimized using numerical simulations. Silver layer thickness above 80 nm is found to yield almost same SPR reflectance spectra with semi-infinite silver layer configuration as shown in Fig. 3.5. As the thickness of the top gold layer is increased, on the other hand, plasmon resonance curve degrades and loses its sharpness as shown in Fig. 3.6. Thus, gold coating thickness is kept as 2 nm in order to satisfy both sensitivity and surface chemistry requirements. Apart from the previous studies which use the Ag/Au bimetallic structure to increase sensitivity [53]–[56], we used this configuration to obtain a response below 520 nm which is not possible with the commonly used single gold layered couplers.

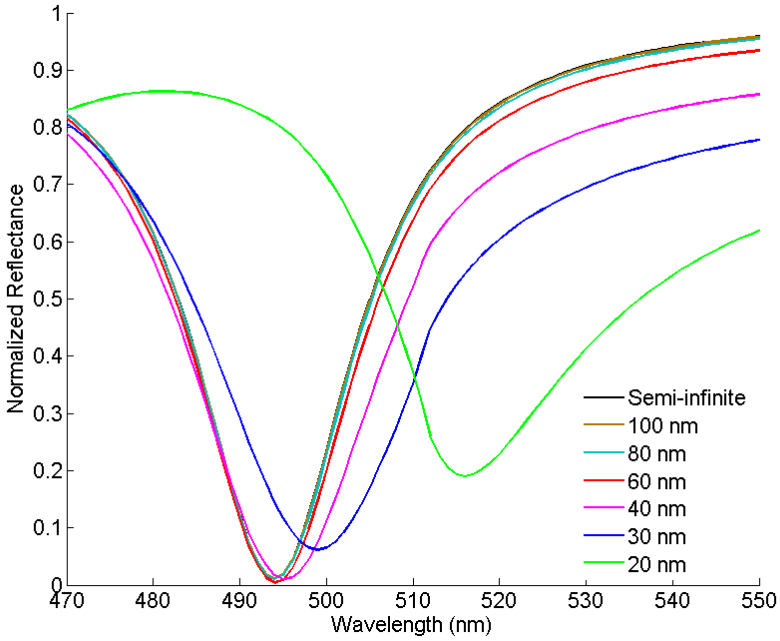

Figure 3.5: Calculated SPR reflectance spectra of Ag coated BD chip under normal incidence of illumination in water medium with respect to decreasing silver thickness. As the thickness of silver layer reduces below 80 nm, SPR curve loses its sharpness due to the interaction of surface plasmon wave with the underlying substrate layer.

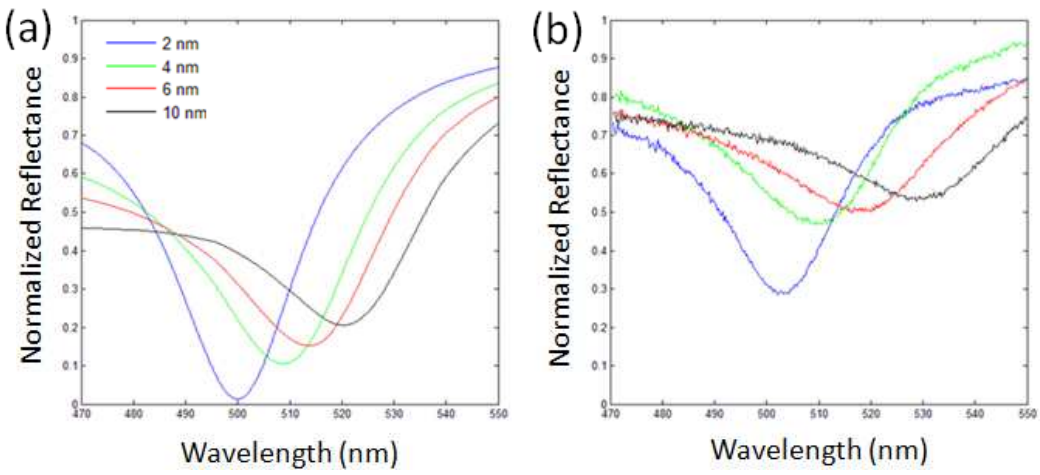

Figure 3.6: Change in SPR reflectance spectra of Ag/Au bimetallic BD chip with respect to increasing top gold layer thickness from 2 nm to 10 nm. (a) Calculated and (b) measured reflectance spectra in water medium at normal incidence. Measurements are taken using normal incidence SPR spectroscopy setup.

Blu-ray discs (BD) are converted to plasmonic surfaces by peeling off the transparent thin protective coating on top of the disc with tweezer after cutting a notch on the side of the disc, followed by metallization using thermal vacuum evaporation (Vaksis Thermal Evaporator). First, a thin germanium layer is deposited to promote better adhesion between BD surface and subsequent metal coating. Germanium (3 nm), silver (80 nm) and gold (2 nm) metal layers are deposited at 0.4 Å/s, 0.6-1.0 Å/s and 0.2 Å/s growth rates, respectively, under 0.005 mTorr chamber pressure. Schematic illustration and SEM image of a Ag/Au bilayer coated BD structure are shown in Fig. 3.7.

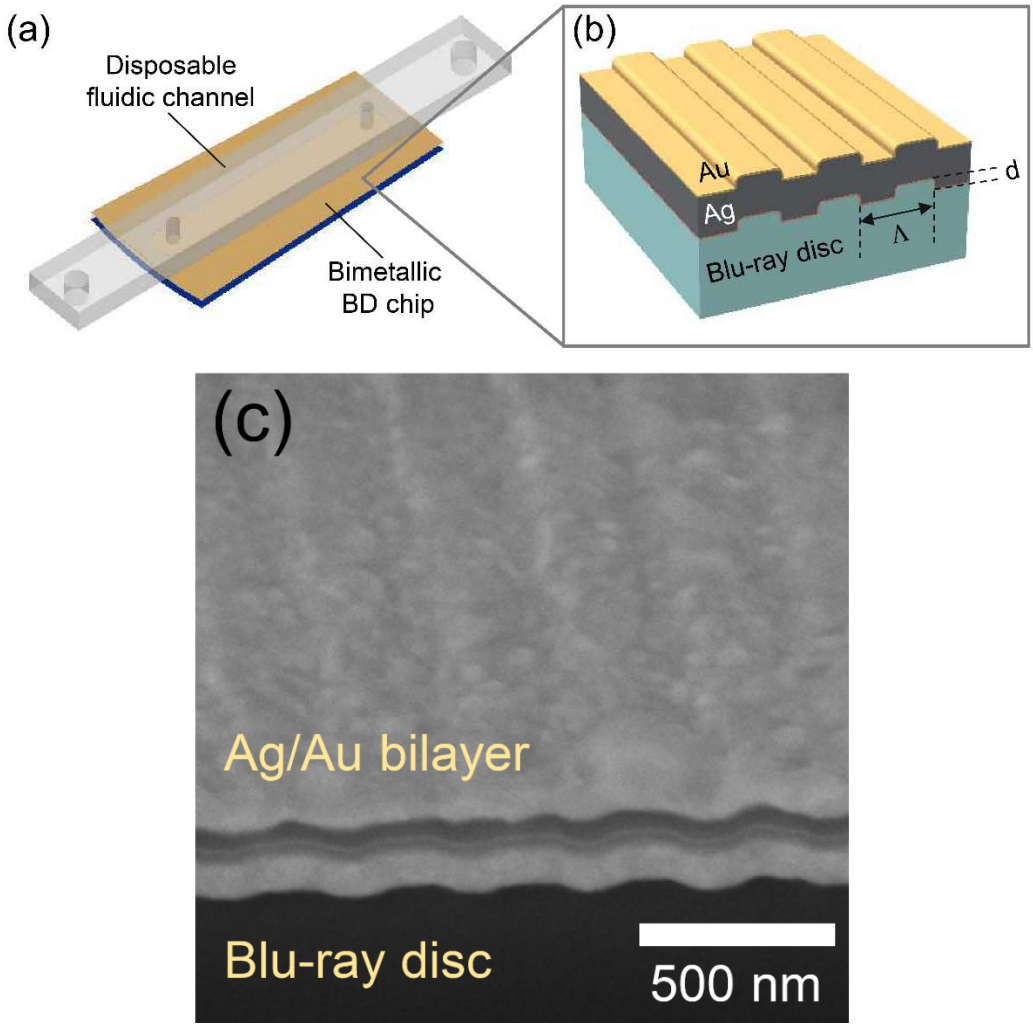

Figure 3.7: Grating coupled SPRi sensor chip. (a) Schematic of the SPRi chip assembly fabricated by integrating a bimetallic Blu-ray disc chip and a disposable fluidic channel. (b) Cross-section schematic view and (c) SEM image of a bimetallic BD chip. Groove depth, d is 20 nm, and pitch width, Λ is 320 nm. Film thicknesses of Ag and Au layers are 80 nm and 2 nm, respectively.

Sensitivity performance of a bimetallic BD based SPR sensor is investigated using numerical simulations. The spectral bulk refractive index sensitivity, $S_{\lambda BC}$ is calculated as 316 nm/RIU. The ratio of the change in resonance wavelength to the change in the thickness of layer formed by the adsorption of molecules onto the sensor surface gives the spectral surface coating sensitivity, $S_{\lambda SC}$, and it is calculated as 0.7 nm/nm for a coating material with n=1.45.

Blu-ray discs as described here allow easy replication of our work by others without needing any infrastructure investment. Moreover, sensor surfaces can be produced at lower costs on a large scale following the manufacturing processes of Blu-ray discs. In fact roll-to-roll printing of gratings is demonstrated [59], which can be used as an alternative to Blu-ray discs. It is important to note that planar sensor surfaces that are fabricated using any of the processes mentioned above are completely compatible with our optical readout configuration.

Implementation of biosensing in real-time without any intervention to the optical alignment of the system during the biomolecular interaction is crucial for reliability and accuracy of the measurement. Incorporation of the sensor chip with a flow cell comes into play in such a case, offering several advantages like enabling the kinetic measurements and fast binding of analytes to the sensor surface, as opposed to the detection in a dry state. However, the integration of the SPR sensor with the flow cell requires leakage-free attachment and off-chip components for plumbing of liquids. During the course of our liquid-based experiments, we have developed 3 different procedures for the fabrication of flow cells, each featuring particular benefits on its own.

The preferred flow cell fabrication technique is an extremely simple, yet very effective method based on laser cutting of a 3 mm thick transparent acrylic plate and a double sided adhesive tape (3M 468MP Adhesive Tape) (Fig. 3.8).

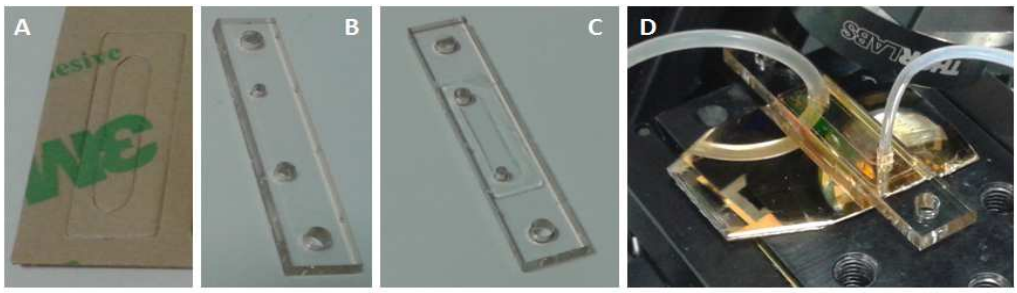

Figure 3.8: Integration of a BD sensor chip with a low-cost microfluidic channel fabricated by laser cutting of transparent acrylic plate and double side adhesive tape. (a) Channel geometry is defined on a double-side adhesive tape using a high power CO_2 laser cutting system. (b) Inlet and outlet holes with conical profile are defined on a 3 mm thick transparent acrylic plate again by laser cutting. (c) First, DST is bond onto the milled acrylic plate. (d) Then, acrylic plate and BD chip are bond together tightly by applying mechanical pressure. Inlet and outlet tubings are mount to the device.

Both channel geometry and holes for inlet and outlet are defined by a high power CO_2 laser cutting system (Epilog Zing 24). Channel geometry is defined on the double sided tape at 8W laser power and 100% scanning speed. Channel frame, inlet and outlet holes are defined on the acrylic plate at 30W laser power and 15% scanning speed. First, double sided tape is bond onto the acrylic plate. Then, acrylic plate and BD chip are bond together tightly by applying mechanical pressure for half a minute. Tygon tubings (Cole-Palmer) are connected to the inlet and outlet of the flow cell. Epoxy adhesive (Bison Epoxy 5 Minutes) is used to completely seal the tubings at the inlet and outlet connections. The volume of a flow cell is 8 microliters (16 x 5 x 0.1 mm^3). An external peristaltic pump is used for controlled plumbing of the liquids through the channel.

The second flow cell fabrication method relies on the use of 3D printing technology based on the fused filament fabrication (FFF) technique as shown in Figure 3.9.

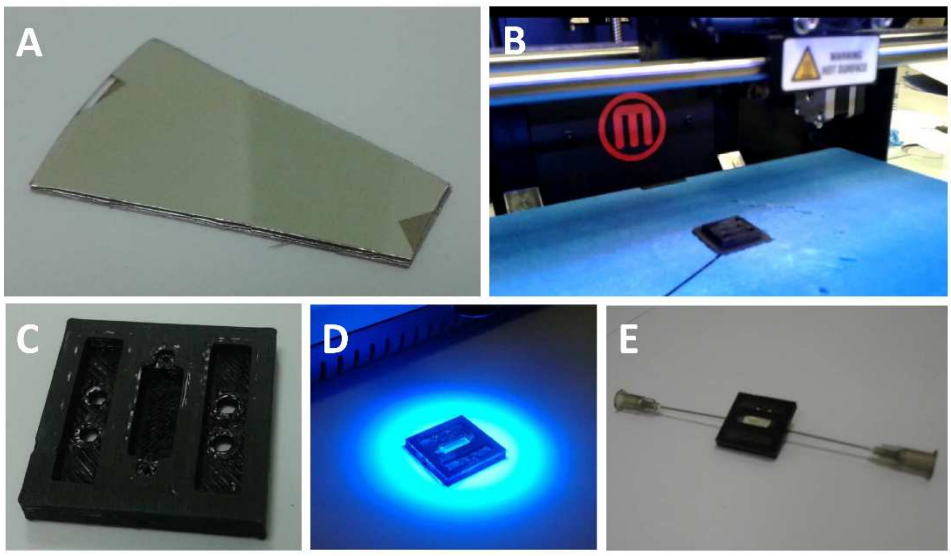

Figure 3.9: 3D printing based fabrication of a flow cell and integration with a BD sensor chip. (a) Flow cell body is designed by a CAD tool and fabricated using a commercial 3D printer out of a PLA filament. (b) Top surface of the flow cell is rubbed with a sandpaper. (c) BD sensor chip is attached with glue inside the channel. A coverglass is bond using UV curable epoxy under UV exposure. (d) Injector needles as inlet and outlet ports are attached to the channel in the same manner with coverglass bonding.

Flow cell body is designed by a 3D modelling CAD tool and fabricated using a commercial 3D printer (MakerBot Replicator 2) out of polylactic acid (PLA) filament at 0.1 mm layer height resolution. Top surface of the flow cell is rubbed with a sandpaper to achieve a finer surface quality. A small piece of BD sensor chip (2x9 mm^2) is attached with glue inside the channel. A cover glass is bond using UV curable epoxy under UV light exposure. Injector needles as inlet and outlet ports are attached to the channel in the same manner with cover glass bonding. Whole the fabrication process from the beginning to the end is completed under 30 minutes per fluidic chip. It seems to be time-saving to fabricate prototype

channels with arbitrarily designed three dimensional geometry, however, time cost increases linearly with the quantity of channels.

The third flow cell fabrication method is a more conventional and well established technique in the microfluidics community which is known as PDMS replication molding (Figure 3.10).

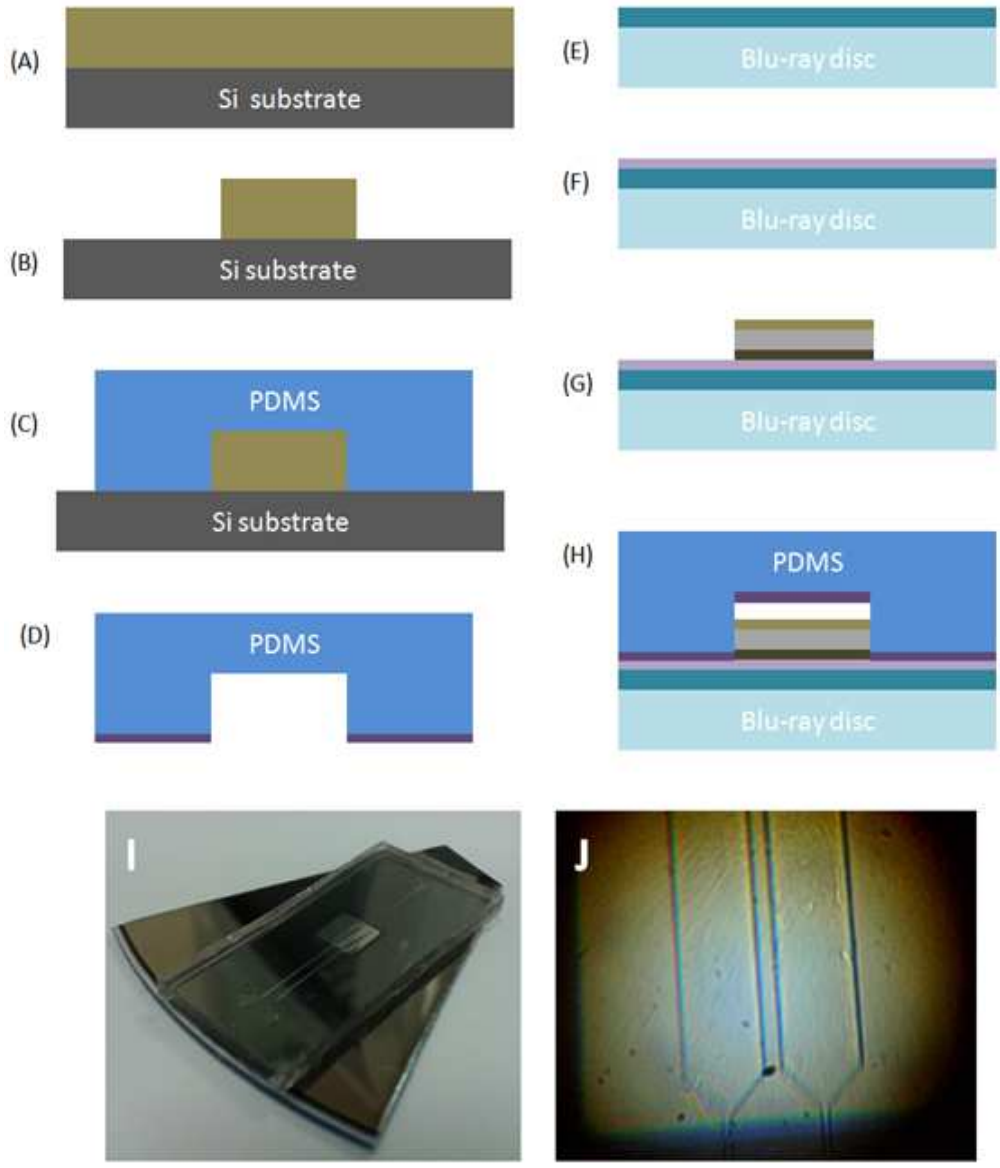

Figure 3.10: PDMS replication molding based fabrication of a flow cell integrated BD chip. (a) SU-8 photoresist is spin-coated on a Si substrate and soft baked on a hotplate. (b) Microchannel geometry is patterned on SU-8 coating by optical lithography followed by post baking and development processes. (c) PDMS-curing agent mixture is poured onto the SU-8 master mold and cured on a hotplate. (d) Hardened elastic PDMS stamp is peeled off gently and treated by air plasma to form hydroxyl groups on the bonding surface. (e) Thin SiO_2 film is deposited on Blu-ray disc substrate using plasma enhanced chemical vapor deposition (PECVD). (f) Hydroxyl groups are formed on the SiO_2 layer by the same air plasma treatment procedure. (g) Ge (3 nm), Ag (80 nm) and Au (2 nm) films are deposited on Blu-ray disc substrate using thermal vacuum evaporation through a shadow mask. (h) PDMS microchannel is bond with Blu-ray chip. (i) Photograph image of a fabricated device. (j) Photograph image taken by measurement setup camera during the liquid flow.

First, SU-8 photoresist (MicroChem SU-8 3050) is spin-coated on a 4 inch Si substrate to yield a uniform 100 um thick film followed by soft baking on a hotplate at 95 C^{o}. Microchannel geometry having two 4 mm long and 1 mm wide channels parallel to each other is patterned on SU-8 coating by optical lithography, post baking and development processes. PDMS and curing agent (Dow Corning Sylgard 184 silicone elastomer kit) are mixed at 10:1 (w/w) ratio and degassed in rough vacuum chamber. PDMS-curing agent mixture is poured onto the SU-8 master mold and cured by heating at 100 C^{o} for 5 hours on a hotplate. Hardened elastic PDMS microchannel stamp is peeled off gently and treated by air plasma with 900 W RF power for 3 sec under rough vacuum environment to form hydroxyl groups on the bonding surface. Inlet and outlet holes are punched using a biopsy punch. In order to bond PDMS microchannel to Blu-ray disc, first, thin (15 nm) SiO_2 film is deposited on a piece of protection layer removed Blu-ray disc using plasma enhanced chemical vapor deposition (Plasma Technology PECVD) at a relatively low plate temperature of 100 C^{o}, at 12 W RF power, and under 1 Torr chamber pressure. Hydroxyl groups are formed on the SiO_2 layer following the same air plasma treatment procedure. Germanium (3 nm), silver (80 nm) and gold (2 nm) metal layers are coated on the Blu-ray disc substrate using thermal vacuum evaporation through a shadow mask. Finally, PDMS microchannel is bond with Blu-ray chip by the virtue of formation of Si-O-Si chemical bonds at the interface of binding surfaces. Although PDMS microchannel based procedure brings up the opportunity of parallel monitoring of a number of channels individually within the scope of imaging optics, it adds more complexities to the fabrication routine. Deposition of a thin SiO_2 film for the formation of hydroxyl groups on top of the chip which is imposed by the bonding chemistry is to name one of them.

3.2.3 Measurement protocol

In a typical measurement, an SPRi sensor chip is plugged into the sample holder unit (Fig. 3.11). Next, LED light source is turned on and polarizing filter is adjusted to transverse electric (TE) polarization where electric field of the transmitted light is parallel to the grating lines of the sensor surface. Inlet port of the flow cell is connected to the pump and outlet port is connected to a waste tube. Flow cell is filled with the running buffer solution. Orientation of the sample with respect to the incident light beam is finely tuned by adjusting set screws behind the sample holder cover until the illumination spot displayed on the touchscreen has a circular shape and gets located at the center of the screen. Having the sample properly aligned, surface image is recorded under TE polarized illumination to be taken as normalization reference. Then the light source is turned off and screen image is captured as dark reading. For the rest of the measurement, the light source is turned on and polarizing filter is adjusted to TM polarization. Before performing the assay protocol, surface image is recorded to establish baseline reading while the sample is in its bare state and surrounded by buffer solution. Intensity change at each pixel is calculated by taking the difference between actual and baseline intensities. Time and area averaging options are provided in the application software to obtain enhanced signal during the course of the measurement. From surface activation to the capture of analyte molecules, the whole assay protocol can be monitored in real-time.

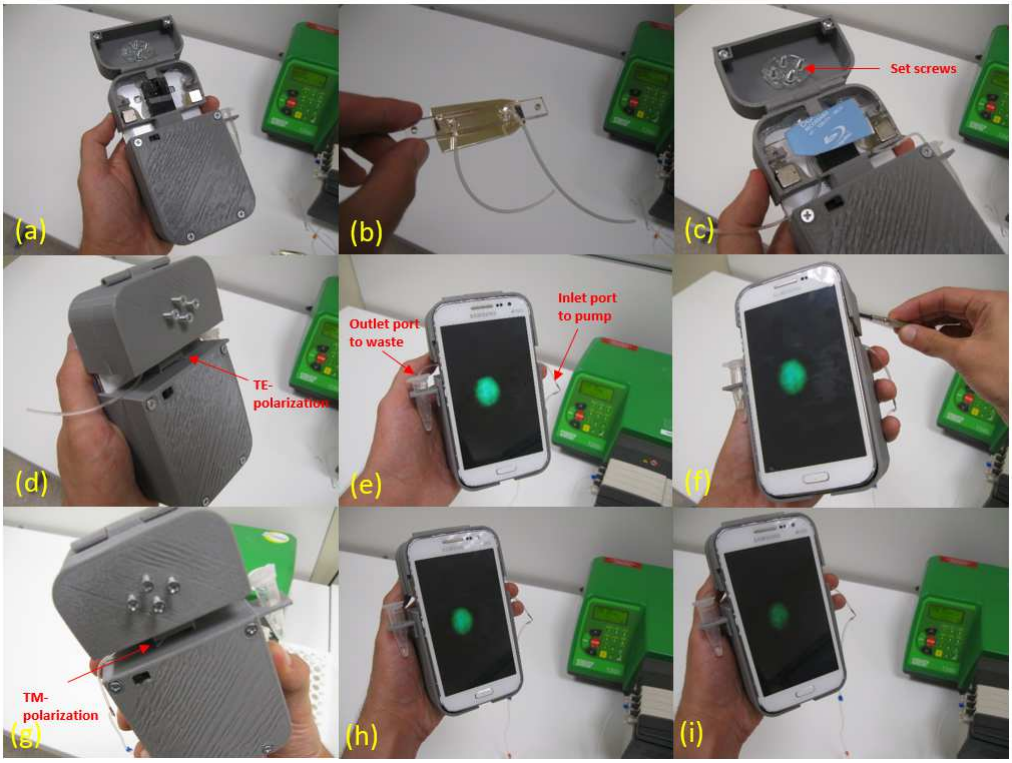

Figure 3.11: A typical measurement protocol. (a)-(c) Plug the SPRi chip into the sample holder unit. (d) Set the polarizer to TE mode (taken as normalization reference). (e) Connect inlet port of the chip to an external pump and inject running buffer. (f) As the flow cell is filled with the liquid, use set screws to align the sample if required. (g) Switch the polarization to TM mode. (h) Follow the assay protocol. (i) Intensity changes (decreases in this configuration) as the molecules attach to the sensor surface.

3.2.4 Experimental setup for wavelength interrogation of plasmon resonance

Reflectance spectra of surface plasmon resonances excited on the sensor chips are probed in real-time using a normal incidence SPR spectroscopy setup (Fig. 3.12). White light emitted from a high power broadband LED source driven by a stable DC current source (Keithley 2400 SourceMeter) is coupled to a multimode fiber optic cable and collimated by a collimation lens at the output of the fiber. Collimated beam of light passes through an adjustable linear polarizer, an adjustable iris to narrow down the beam diameter, and a non-polarizing beam splitter cube. Polarized and narrowed beam is reflected off the sensor surface, directed by the beam splitter towards the spectrometer fiber optic components, collected by a fiber coupling lens and analyzed by a spectrometer (Ocean Optics Maya 2000 Pro). Each reflectance spectrum measurement is taken at 20 ms of integration time.

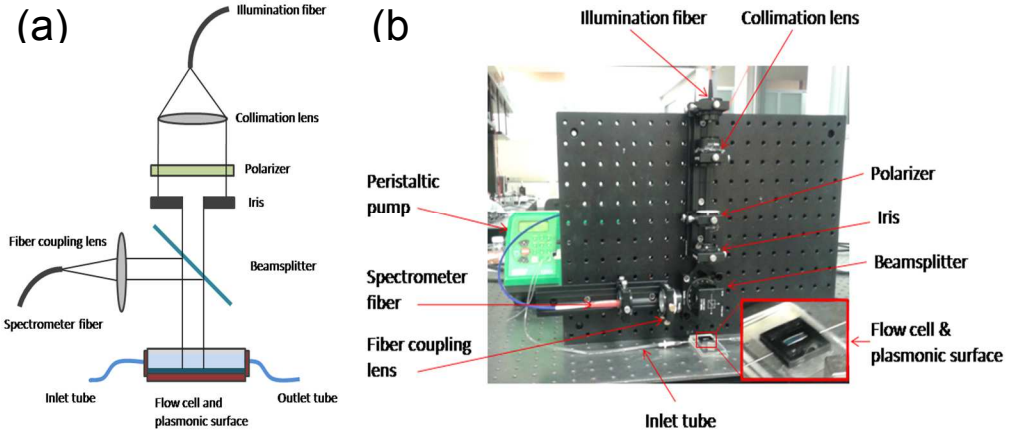

Figure 3.12: Experimental setup for the wavelength interrogation of plasmon resonance. (a) Schematic representation and (b) photograph of the optical configuration.

Plasmon resonance curve information needs to be extracted from raw spectrum data which contains emission spectrum of the light source and the dark current generated in the detector elements of spectrometer (Fig. 3.13). Since surface plasmons are excited by a TM-polarized illumination in a 1D grating coupling scheme, it is common to use TE-polarized spectrum as reference of normalization. To eliminate the dark current effect, background spectrum taken in the absence of illumination is subtracted from each spectra. Hence, normalized reflectance spectra, $R(\lambda)$ is calculated using;

$$R(\lambda) = \frac{R_{TM}(\lambda) - D(\lambda)}{R_{TE}(\lambda) - D(\lambda)} \tag{3.1}$$

where $R_{TM}(\lambda)$ is the reflected spectrum at TM polarization, $R_{TE}(\lambda)$ is the reflected spectrum at TE polarization and $D(\lambda)$ is the spectrum reading in the absence of illumination.

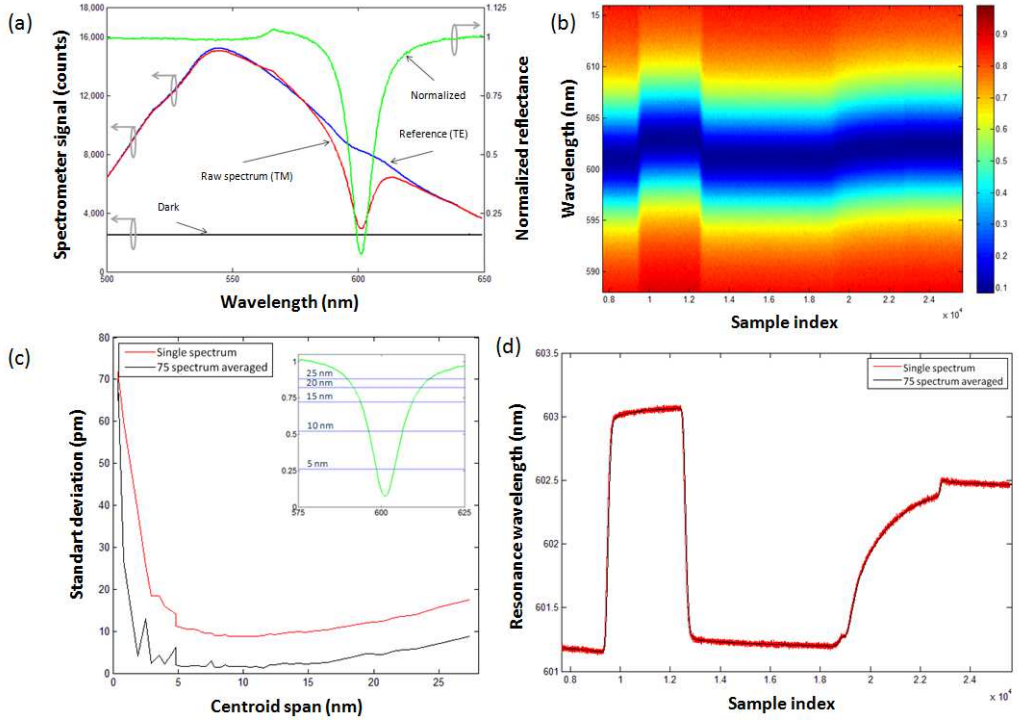

Figure 3.13: Data analysis steps of time-resolved spectral interrogation measurements. (a) Calculation of the normalized reflectance spectrum by taking the ratio of background corrected TM and TE polarized spectra. (b) Spectrogram showing the change in the resonance curve over time. (c) Optimization of the centroid algorithm. (d) Sensorgram generated using centroid method.

The spectral position of the resonance dip is probed using centroid algorithm [60]. In centroid algorithm, centroid value, C, is calculated by;

$$C = \frac{\sum_i i(x_{th} - x_i)}{\sum_i (x_{th} - x_i)} \tag{3.2}$$

where x_i is the signal at pixel *i* for CCD pixels having signal below a certain threshold value (x_{th}) around the resonance curve. Centroid value is not exactly equal to the resonance wavelength due to the asymmetric shape of the resonance curve, but a reliable indicator to probe the resonance dip by adding up the contributions of a set of points around the resonance curve and thereby enhancing the spectral sensitivity beyond the resolution limits of the spectrometer itself. Standard deviation of the centroid signal is dependent on the threshold value).

Threshold value that gives the lowest standard deviation is found to be around 0.5. Time-averaging is another factor that enhances the sensitivity significantly by reducing the noise.

Resonance wavelength shift noise of a spectrogram averaged over 75 spectra is calculated as 1.5 pm. By taking the experimental spectral bulk refractive index sensitivity, $S_{\lambda BE}$ as 356 nm/RIU for BD SPR sensors, the minimum detectable bulk refractive index change, σ_{nBE} is found as 4.2 x 10^{-6} RIU for the wavelength interrogation setup.

3.2.5 Optimization of the illumination wavelength

Although all BDs share the same periodicity and depth values in compliance with the industrial standards, there exists slight variations in the ridge widths among different brands which in turn plasmon resonance wavelength takes different values between 470 nm and 520 nm under normal illumination condition which is attributed to the formation of plasmonic band gap as depicted in Fig. 3.14.

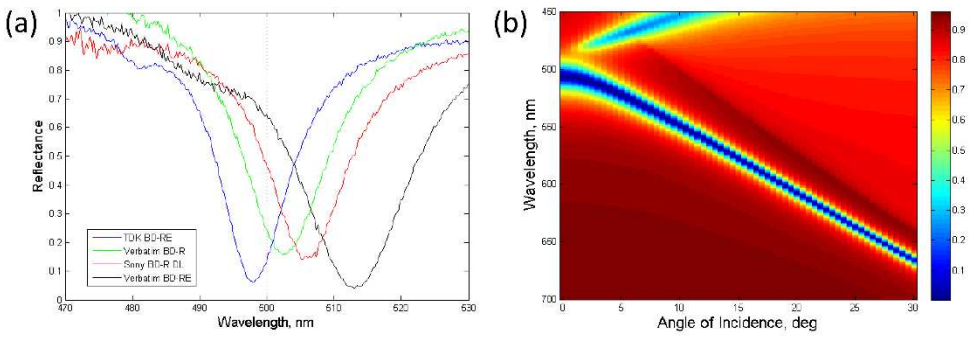

Figure 3.14: (a) Reflectance spectra of different brands of BD chips, (b) Calculated reflected spectra with respect to angle of incidence of a particular BD chip.

This variation in the position of resonance curve dictates significant constraint to the intensity interrogation scheme as in our case such that illumination wavelength at which reflected intensity measurements are taken has to be determined separately for each brand. The illumination wavelength (λ_i) of the imaging platform which yields the highest intensity sensitivity was identified by measuring reflectance spectra for varying refractive indices of the surrounding liquid medium (Fig. 3.15).

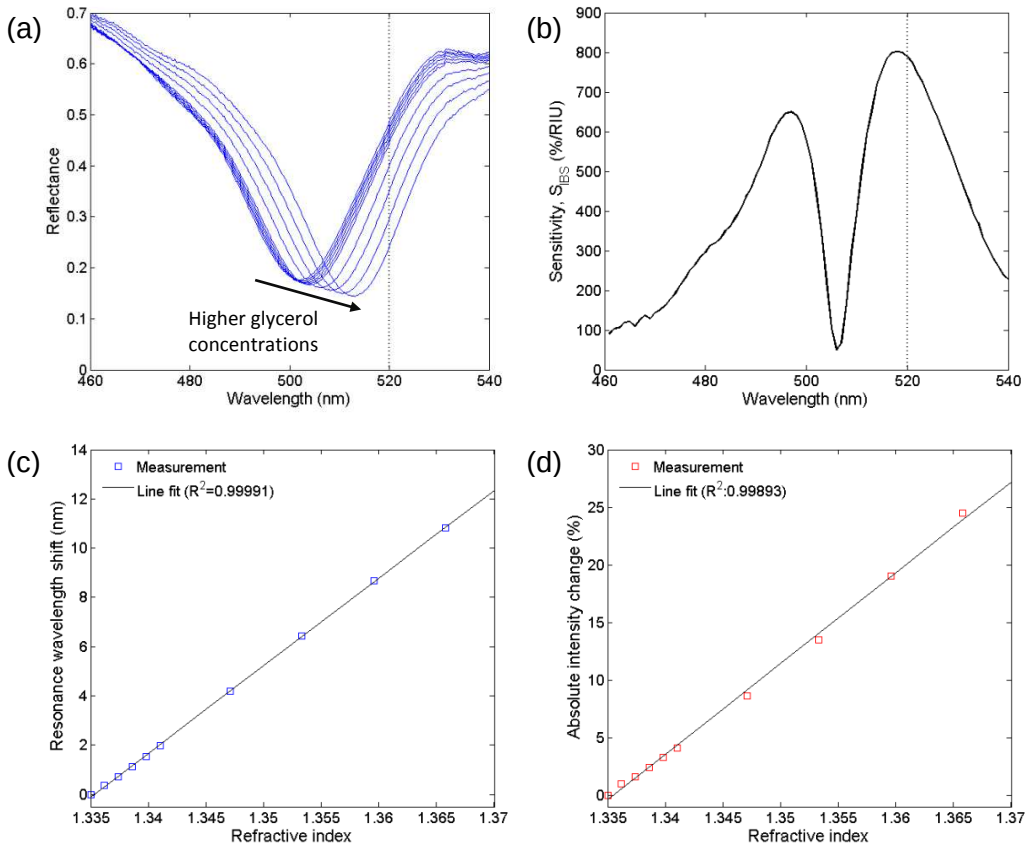

Figure 3.15: Optimization of the illumination wavelength. (a) Resonance wavelength shift depending on the refractive index of the glycerol solution at increasing concentrations from 1% to 25% v/v. (b) Bulk refractive index sensitivity with respect to the illumination wavelength. Calibration curves for the resonance wavelength shift (c) and intensity change (d) obtained from the wavelength interrogation setup. The experimental spectral bulk refractive index sensitivity, $S_{\lambda BE}$ is found as 356 nm/RIU.

Liquid solutions with refractive indices ranging from 1.335 to 1.365 were prepared by dissolving glycerol (n=1.474) in deionized water (n=1.335) at varying concentrations. The highest bulk refractive index sensitivity was found to be about 800 %/RIU at the wavelength of 520 nm for TDK BD-R substrate. Both resonance wavelength shift and intensity change (λ_i=520 nm) show linear dependence on the refractive index change within the $1.335 < n < 1.365$ range.

3.2.6 Chemical materials

RAM IgG and mouse IgG were purchased from Stratech Scientific Ltd. Jackson ImmunoResearch. 11-mercaptoundecanoicacid (11-MUDA), phosphate-buffered saline (PBS), TWEEN® 20, sodium acetate trihydrate, glacial acetic acid, N-hydroxysuccinimide (NHS), ethanolamine, and bovine serum albumin (BSA) were purchased from Sigma-Aldrich. 1-Ethyl-3-(3 dimethylaminopropyl)-carbodiimide (EDC) was purchased from Pierce-Thermo Scientific. All other chemicals were of analytical grade.

One PBS tablet is dissolved in 200 mL of deionized water to obtain a 10 mM PBS running buffer (pH 7.4, 0.0027 M potassium chloride and 0.137 M sodium chloride). In order to prepare sodium acetate buffer solution at desired molarity and pH values, first 2.72 g of sodium acetate trihydrate (MW:136.08 g/mol) is dissolved in 200 mL of deionized water, and 114 uL of glacial acetic acid (17.47 M) is diluted in 20 mL of deionized water. 0.1 M sodium acetate solution and 0.1 M acetic acid solution are mixed at 10:1 (v/v) ratio to yield 0.1 M sodium acetate buffer solution at pH 5.6. PBS buffer with TWEEN® 20 detergent (PBS/T) (0.05%) is prepared by adding 50 uL of TWEEN® 20 to 99.95 mL of PBS buffer.

3.3 Results and discussion

3.3.1 Microarray imaging of Ag/Au bimetallic sensing spots

We have performed SPR imaging of Ag/Au bimetallic microspot array under bulk dielectric media with changing refractive indices. The bimetallic microarray structure was fabricated using conventional optical lithography processes in addition to metal deposition steps. The diameter of each spot is 110 μm and the spacing between adjacent spots is 130 μm. First, we have recorded video of illuminated sensor surface at 30 frames/second during the successive flow of glycerol solutions with increasing refractive indices. Each 200 consecutive video frames were averaged in order to enhance the signal-to-noise ratio. As the refractive index of the surrounding medium gets higher, plasmon resonance curve shifts towards longer wavelengths resulting in darker imaging spots under TM polarized illumination. Fig. 3.16a shows green channel view of an averaged RGB image of a microspot sensor array in 20% v/v glycerol solution environment (n_d=1.3596). SPRi difference images were generated by taking TE images as normalization reference, and TM images in pure water medium as background (Fig. 3.16b). Line profile of a row of microarray reveal the uniformity of the reflectivity change across the spots (Fig. 3.16c). Average reflectivity change of spots were measured at each glycerol concentration level from 1 % to 25 % v/v. The glycerol calibration curve for 4x4 spots located within the rectangular frame shown in Fig. 3.16a exhibits high linearity (R^2=0.9951) within a dynamic range of 22200 x 10^{-6} RIU between n_d=1.3354 and 1.3576 (Fig. 3.16d). The error bars shown in Fig. 3.16d show twice the standard deviation (2SD) of the measured value demonstrating the low intra-sensor variability between 16 spots. The slope of the calibration curve which gives the experimental reflectivity bulk refractive index sensitivity, S_{RBE} was found as 485 %/RIU. Time resolved SPR responses of individual sensing spots shown in Fig. 3.16a are plotted in Fig. 3.17. Intensity noise of a single pixel in terms of percentage reflectivity, σ_R was found as 0.2 %, whereas averaging a rectangular area of 10-by-10 pixels (120 x 120 μm^2) reduces

the reflectivity noise down to 0.02 % level. Thus, minimum detectable bulk refractive index change, σ_n over a 10-by-10 pixels area is calculated as 4.12 x 10^{-5} RIU for the smartphone platform. The low cost Ag/Au bimetallic BD SPR structure exhibits relatively low refractive index sensitivity as compared to the previously reported SPR grating, prism and waveguide couplers [4], [61]–[64]. However, since the noise level is also reduced by area averaging, overall resolution of the system is comparable with the previously demonstrated studies.

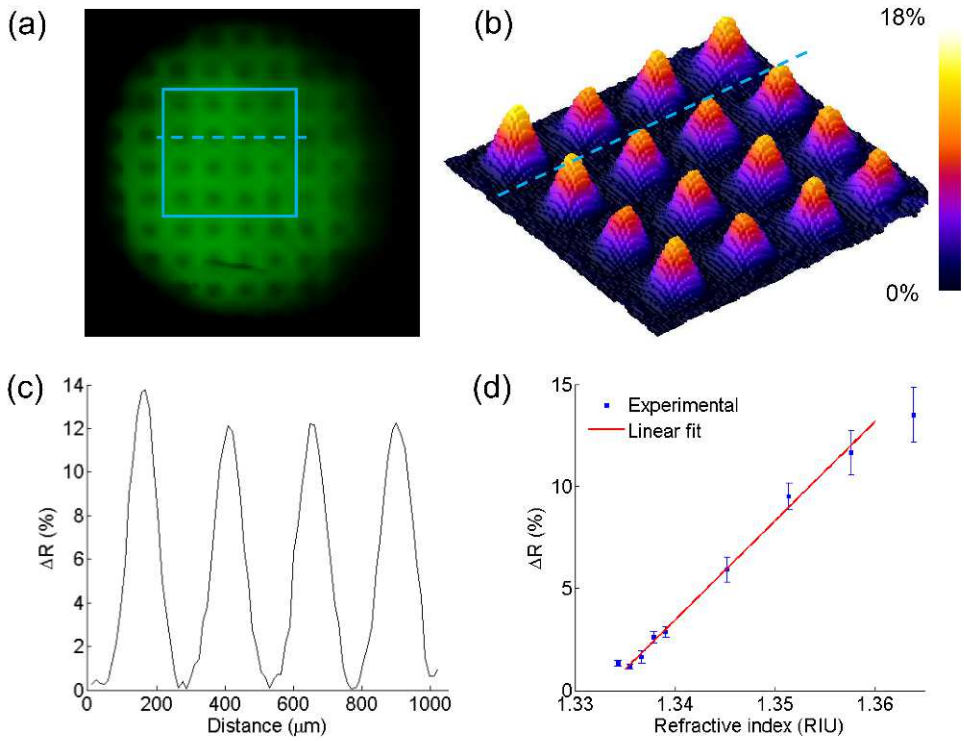

Figure 3.16: Microarray imaging of sensing spots under bulk dielectric media with different refractive indices. (a) Green channel view of an RGB image of a microarray of Ag/Au bimetallic sensing spots under 20% v/v glycerol solution environment (Refractive index of glycerol solution, n_d:1.3596). (b) 3D representation of SPRi difference image. Baseline image is taken under pure water medium (Refractive index of pure water, n_d:1.335). (c) Line profile of a row of microspots. (d) Percentage reflectivity change with respect to the refractive index of bulk medium at varying concentrations of glycerol solutions from 1% to 25% v/v. Bulk refractive index sensitivity obtained from linear calibration curve is 485 %/RIU. Error bars denote 2SD of measurements from 16 spots shown in part (a), demonstrating intra-sensor variability.

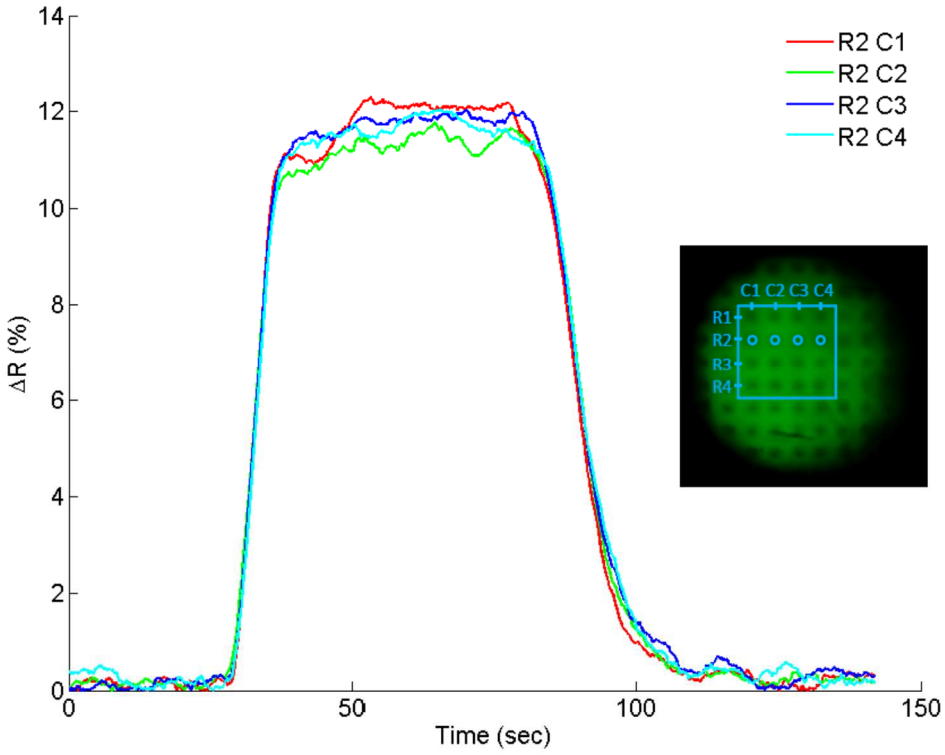

Figure 3.17: Sensorgrams showing average reflectivity changes of individual sensing spots during fluid exposures. The fluidic channel is initially filled with pure water (refractive index of pure water, n_d:1.335) and sensor responses are taken as baseline signals. Then, 20% v/v glycerol solution (refractive index of glycerol solution, n_d:1.3596) is injected onto the microarray surface at 50 µL/min flow rate for 50 seconds. Finally, glycerol solution in the channel is replaced with pure water to return into the initial fluidic state. Circular ROIs overlaid on the inset figure denote the locations of 4 sensing spots on the green channel SPR image where R stands for row and C stands for column positions. Video data is recorded at 30 frames/second rate and averaged over 200 consecutive frames.

3.3.2 Real-time monitoring of bovine serum albumin (BSA) adsorption

We have taken time-resolved intensity change measurements in response to the protein adsorption on the sensor surface. Bovine serum albumin (BSA) is known to adsorb onto the gold surface forming a 4-7 nm thick monolayer [65]. 1 mg/ml (15 μM) BSA (Sigma Aldrich) dissolved in 10 mM phosphate buffer solution (PBS, pH=7.4) was injected through the flow cell for 5 min after a thorough PBS wash. Following the formation of self-assembled monolayer on the gold coating, the sensor surface was cleaned by PBS wash again. SPRi difference image of arbitrarily defined 4-by-4 rectangular region of interests after the BSA adsorption is shown in Fig. 3.18a.

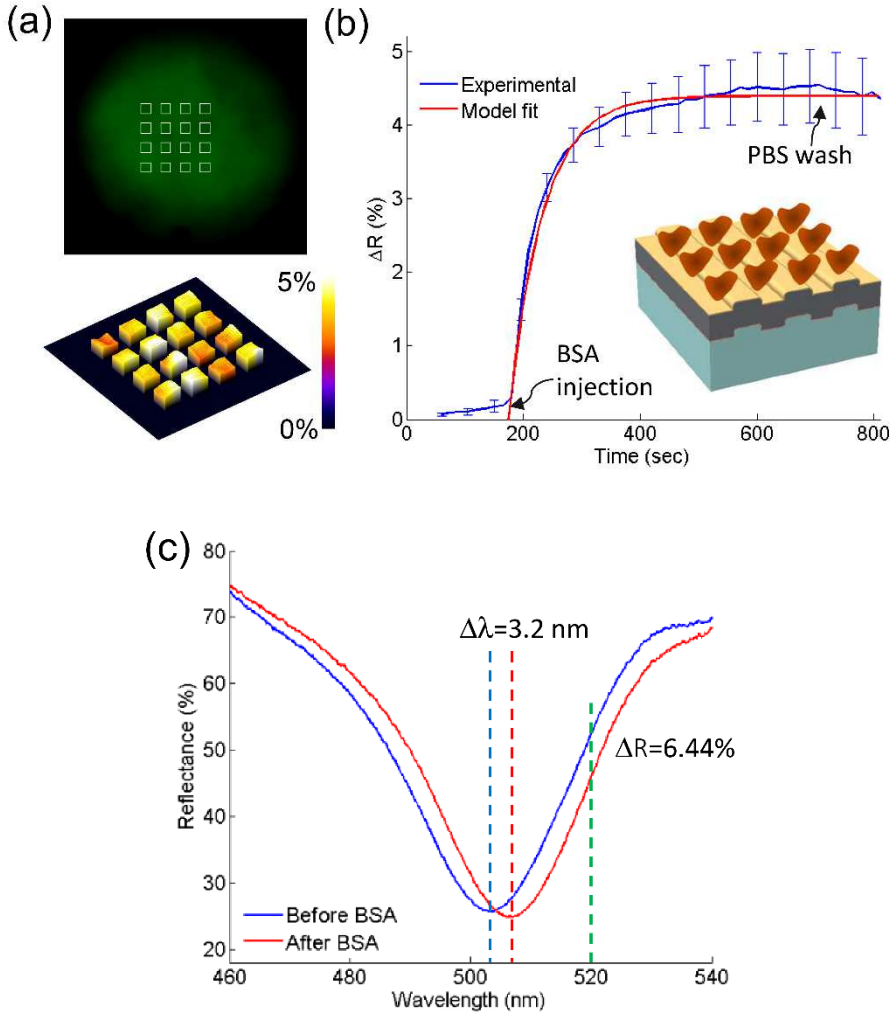

Figure 3.18: Real-time monitoring of BSA adsorption onto the gold surface. (a) Arbitrarily defined 4-by-4 rectangular region of interests (96 x 96 μm^2 each) on entirely Ag/Au bilayer coated sensor spot image (top) and background corrected SPRi difference image of ROIs (bottom) taken after BSA adsorption. (b) Sensorgram showing average reflectivity change of ROI spots during the implementation of BSA protocol. The inset schematic illustrates binding of BSA molecules on the grating surface. Error bars denote 2SD of measurements from 16 spots. (c) Reflectance spectra taken before and after BSA adsorption using the normal incidence SPR spectroscopy setup.

Average reflectivity change of 16 ROIs over time is as shown in Fig. 3.18b and the steady-state reflectivity difference is found as 4.37±0.53%. Resonance wavelength shift caused by the BSA adsorption was measured using SPR wavelength interrogation setup repeating the same BSA protocol. The resonance dip shifts from 503.8 nm to 507 nm as shown in Fig. 3.18c. Reflectivity at 520 nm decreases by 6.44% from 52.46% to 46.02%, in agreement with imaging results. Sensorgram of BSA adsorption onto the gold sensor surface monitored by SPR wavelength interrogation setup is shown in Fig. 3.19.

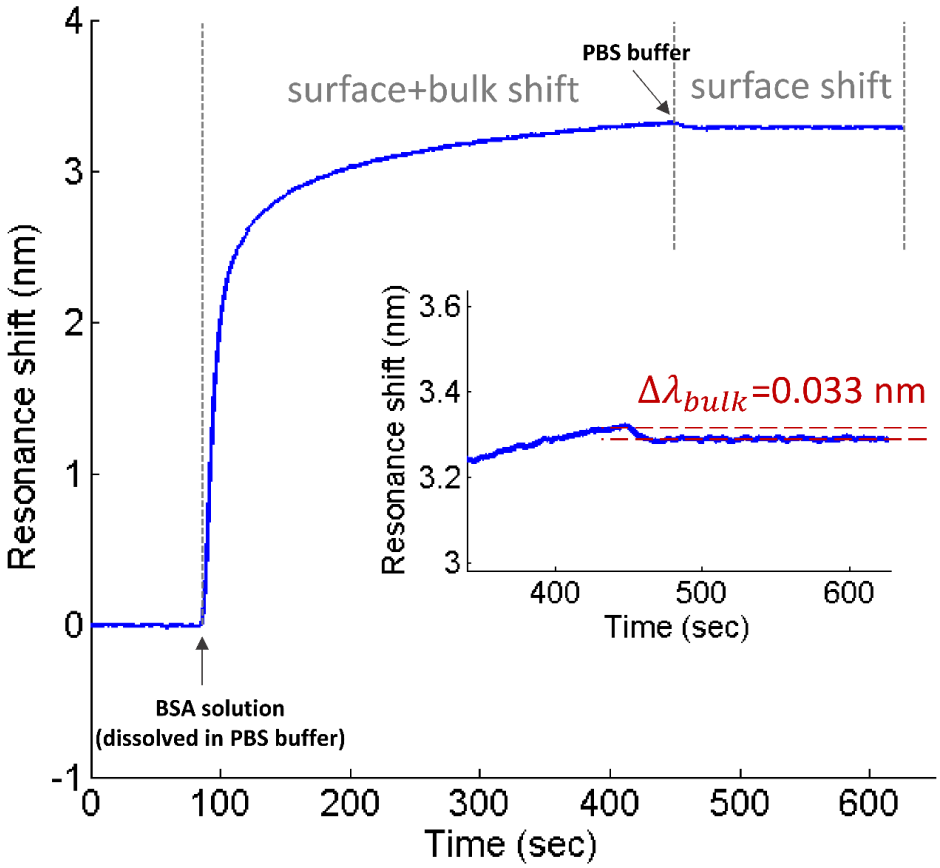

Figure 3.19: Sensorgram of BSA adsorption onto the gold sensor surface monitored by SPR wavelength interrogation setup. The sensorgram response during the association phase (between the injection of BSA solution and PBS buffer wash) is due to the overall resonance shift, $\Delta\lambda_{total}$ caused by both surface shift, $\Delta\lambda_{surface}$ (BSA adsorption) and bulk shift, $\Delta\lambda_{bulk}$ (refractive index difference of solutions). Inset figure depicts resonance wavelength difference, $\Delta\lambda_{bulk}$=0.033 nm following the PBS wash which is due to the small refractive index difference between BSA and PBS buffer solutions ($\Delta n = 93 \times 10^{-6}\ RIU$).

We have performed kinetic analysis of the reaction based on a simple interaction model described below:

$$\text{Reaction: } A + B \rightarrow AB \tag{3.3}$$

$$\text{Rate of association: } \frac{d[AB]}{dt} = k_a[A][B] \tag{3.4}$$

where A represents the BSA protein dissolved in the injected BSA solution, B is the available binding site on the gold sensor surface, and AB is the complex formed by the adsorption of BSA onto the gold surface. The rate of complex formation in terms of reflectivity change ($\Delta R(t)$) can be expressed as,

$$\Delta R(t) = \Delta R_{max}\left(1 - e^{-k_a[A]t}\right) \tag{3.5}$$

where ΔR_{max} is the maximum reflectivity change, k_a is the association rate, and [A] is the concentration of the binding analyte. The association rate, k_a of the BSA-Au complex formation is calculated as 1150 $M^{-1}s^{-1}$, with the assumption that the dissociation rate, k_d is negligibly small as can be deduced from the sensorgram curve after second PBS injection.

3.3.3 Demonstration of a biodetection assay

As an exemplary biodetection experiment, capture of mouse IgG antibody by immobilized layer of rabbit anti-mouse (RAM) IgG antibody protocol was implemented as direct assay (Fig. 3.20).

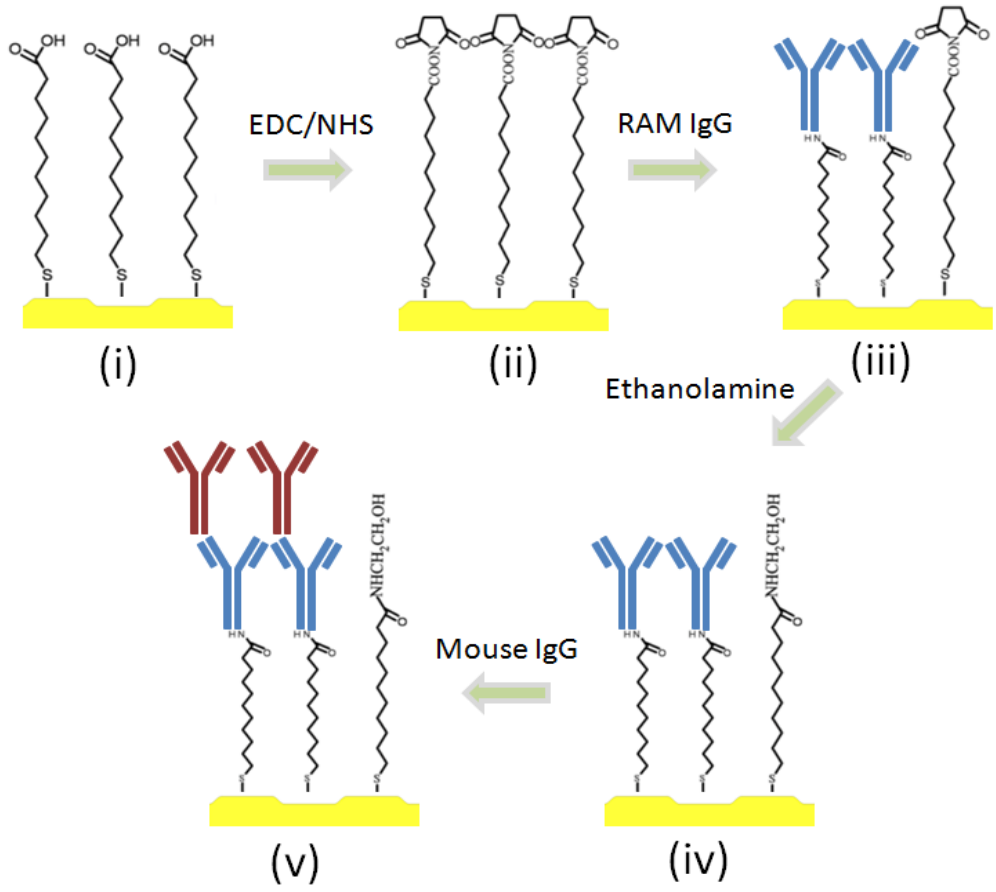

Figure 3.20: Surface modification of Blu-ray disc plasmonic chips. (i) 11-MUDA SAM formed on thin gold film coated chip. (ii) SAM layer is activated by exposing EDC/NHS mixture. (iii) RAM IgG antibody is immobilized on the activated surface by amine coupling chemistry. (iv) Non-reacted NHS esters were capped with ethanolamine solution to block non-specific analyte bindings. (v) Capture of mouse IgG antibodies by RAM Fc immobilized sensor surface.

First, surface of a thin gold film coated BD chip was cleaned by argon plasma treatment. Sensor surface was coated with self-assembled monolayer (SAM) of 11-mercaptoundecanoicacid (11-MUDA) by immersing the chip in 2 mM ethanol solution of mercaptoundecanoic acid overnight followed by rinsing with ethanol and water, and drying in the fume hood. Then, BD chip was integrated with a flow cell. Ethanol (70%) and PBS solutions were injected onto the surface at 100 μL/min flow rate for further cleaning. Surface of the 11-MUDA SAM layer was activated by the exposure of 400 mM 1-Ethyl-3-(3 dimethylaminopropyl)-carbodiimide (EDC) and 100 mM N-hydroxysuccinimide (NHS) mixture (1:1) at 100 μL/min flow rate for 4 min. Both reagents were prepared in distilled water and mixture was prepared just before use. Diluted RAM IgG (50 μg/mL) in 0.1 mM sodium acetate buffer solution was injected onto the activated sensor surface at 50 μL/min flow rate for 3 min. RAM IgG antibodies were immobilized on the activated surface by amine coupling chemistry. Following the RAM Fc immobilization, non-reacted NHS esters were capped by the exposure of 1 M ethanolamine solution at 100 μL/min flow rate for 4 min to prevent non-specific analyte bindings. Sensor surface was cleaned by PBS wash for 5 min after each step. The whole immobilization process from surface activation to blocking step was probed in real-time using the wavelength interrogation setup (Fig. 3.21a).

SPR chip immobilized with RAM IgG is taken out the spectral interrogation setup and plugged into the smartphone attachment. Mouse IgG solutions at concentrations ranging from 1.33 nM to 830 nM were injected successively at 50 μL/min flow rate for 5 min. Intensity changes of individual pixels at three distinct locations on the sensor surface is shown in Fig. 3.21b. Dose-response curve reveals that nanomolar level detection of antibody analyte is achievable within a dynamic range from a few nanomolars to micromolar concentration.

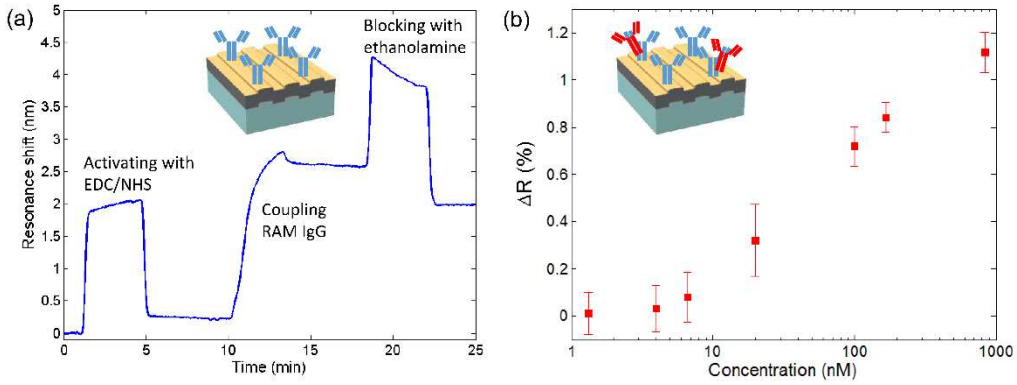

Figure 3.21: Nanomolar level detection of capture of mouse IgG by immobilized layer of RAM IgG (a) Spectral sensorgram showing the immobilization steps of RAM IgG taken by using the normal incidence SPR spectroscopy setup. (b) Dose-response curve for the capture of mouse IgG taken by using SPR imaging platform. The inset schematics illustrate immobilization of RAM IgG (blue colored) on the sensor surface and selective binding of mouse IgG (red colored) with RAM IgG, respectively. Error bars denote 2SD of measurements from 3 spots.

3.4 Conclusion

In this work, we demonstrated the use of a smartphone as a hand-held surface plasmon resonance imaging biosensor with high sensitivity. Developing an attachable imaging accessory from inexpensive optical components and 3D printed parts, and using easy-to-implement procedures for fabricating miniaturized sensor chips integrated with flow cells from extremely cheap substrates like optical storage discs, we offer a promising detection platform that enables biosensing in the field with high level of portability and affordable cost (See Table 3.1 for a detailed comparison of our work with other cell phone based SPR biosensors). The capability to perform parallel assays in a short amount of time allows the use of the instrument for point-of-care applications where monitoring of multiple parameters is desirable.

Table 3.1: Comparison of cell phone based SPR biosensors

Paper	**This work**	**Preechaburana et al.** [50]	**Liu et al.** [14]	**Bremer et al.** [51]	**Roche et al.** [15]	**Dutta et al.** [52]
SPR interrogation scheme	Intensity modulation (imaging)	Intensity modulation (angle-resolved)	Intensity modulation	Wavelength modulation	Intensity modulation	Wavelength modulation
Number of readout channels	>20.000 individual pixels over 3 mm^2 sensor area (2D resolved)	20 (1D resolved)	3	1	1	1
SPR coupling mechanism	Grating	Prism	Waveguide	Waveguide	Localized SPR	Localized SPR
Transducer element	Blu-ray disc	PDMS prism	Silica capillary	PCS fibre	Gold nanorods	Gold nanoparticles
Illumination source	Single color LED	Built-in screen	Built-in flash LED	Built-in flash LED	Tri-color LED	External broadband source
Data acquisition and analysis	Custom developed Android application	Custom developed iOS application	Custom developed Android application	Standard camera app & computer software	Standard camera software & computer software	Standard camera app & computer software
Sample handling	Single-channel flow cell	Single-channel flow cell	Single-channel flow cell	Liquid chamber	Quartz cuvette	Quartz cuvette
Analyte(s)	Glycerol solution, Bovine serum albumin (BSA), Mouse immunoglobulin G	Ethanol solution, β2 microglobulin	NaCl solution, Bovine immunoglobulin G	Glycerol solution	Monocyte chemoattractant protein-1 (CCL2)	Bovine serum albumin (BSA), Trypsin enzyme
Sensitivity	485 %/RIU	-	1136 %/RIU	5.96 x 10^{-4} RIU/pixel	0.8 AU.μg^{-1}.mL	17.466 nm.mg^{-1}.mL (BSA), 13.063 nm.mg^{-1}.mL (Trypsin)
Resolution (RIU) or LOD (µg/mL)	4.12 x 10^{-5} RIU	2.14 x 10^{-6} RIU	7.4 x 10^{-5} RIU	-	0.099 µg/mL	19.2 µg/mL (BSA), 25.7 µg/mL (Trypsin)

Chapter 4

Infrared absorption spectroscopy on a mobile phone

4.1 Introduction

Infrared absorption spectroscopy has been widely employed in the identification and quantitative analysis of chemical substances [66]. Implementation of such analysis is mainly performed by using bulky bench top instruments in advanced laboratory settings. Collection and transportation of analyte samples from the areas of interest to the measurement units brings some additional technical challenges and increases turnaround times. Besides aforementioned infrastructure requirements and time related costs, it becomes crucial to be able to perform such analysis in the field in some cases such as the detection of hazardous gases, explosive vapors, volatile organic compounds (VOCs) etc. Nondispersive infrared (NDIR) sensors as portable and field deployable devices have been demonstrated so far to detect some gases including NO, SO_2, CO_2, CO and CH_4. Recently, optoelectronic noses that utilize infrared absorption in the mid-IR range have been proposed to detect VOCs [67], [68] and chemical warfare agents [69]. All of these

studies demonstrate single or a certain number of chemical sensing since they are designed to take IR absorption measurements at single or a limited set of bands. In order to feature the full benefits of IR absorption spectroscopy for on-site chemical analysis, miniaturized IR spectrometer designs that are capable of producing spectroscopic data with enhanced resolution and sensitivity need to be developed.

Here, we present IR absorption spectroscopy on a mobile phone. We have developed a compact spectrometer system that hosts a miniature and mobile platform compatible uncooled IR camera, custom-fabricated silicon transmission diffraction grating and 3D-printed optomechanical components. Proof-of-principle experiments have been conducted by passing IR radiation emitted from a rod shaped IR source through a polymeric film, and analyzing the transmitted radiation by collecting with the spectrometer apparatus. Our results demonstrate that our miniaturized IR spectrometer design could pave the way for low-cost, portable and quick analysis of a large set of chemical substances in the field settings without requiring any disposables.

4.2 Materials and Methods

4.2.1 Spectrometer configuration for IR absorption spectroscopy

Infrared radiation emitting from a thin glow bar is passed through a sample of interest (Fig. 4.1a). Electromagnetic wave is absorbed by the sample material according to the relation described by the Beer-Lambert law,

$$A(\lambda) = \varepsilon(\lambda)cl \tag{4.1}$$

where $A(\lambda)$ is the absorbance, $\varepsilon(\lambda)$ is the molar absorptivity, c is the concentration, l is the optical pathlength of the sample and λ is the wavelength of the electromagnetic radiation. Transmitted radiation is then passed through a

transmission diffraction grating in order to disperse its wavelength components across an infrared sensitive photodetector array. Infrared absorption spectra is obtained by measuring intensity level at each detector element and using

$$A(\lambda) = -log\big(T(\lambda)\big) \tag{4.2}$$

where $T(\lambda)$ is the fraction of transmitted intensity.

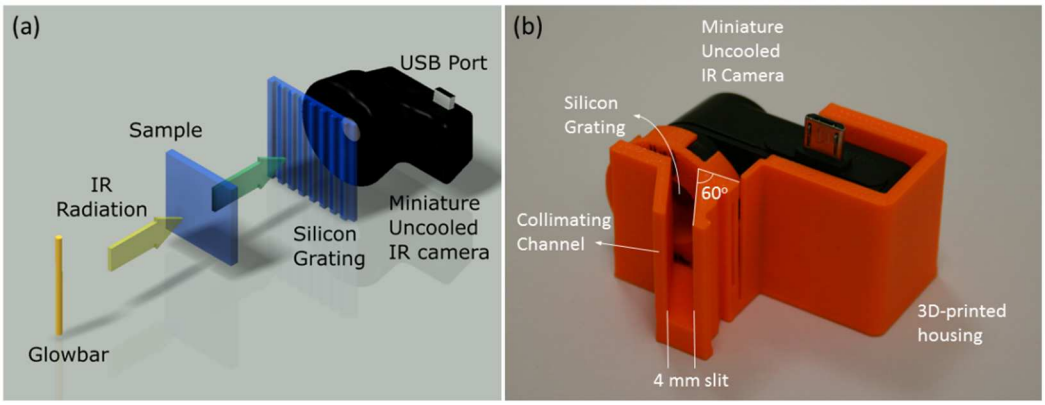

Figure 4.1: (a) Schematic illustration of IR absorption spectroscopy using a miniature uncooled IR camera. (b) Photograph of the 3D-printed spectrometer apparatus.

4.2.2 Uncooled thermal cameras as photodetector arrays

Uncooled thermal cameras are viewed as low-cost and light-weight solutions for radiation detection within the infrared spectral region. Along with the release of mobile platform compatible thermal cameras [70], [71], infrared radiation detection has become realizable in a portable and easily accessible manner. The operation principle of these cameras relies on vanadium oxide (VOx) based bolometric detection. In a typical bolometer, absorbed infrared radiation changes the temperature of a suspended sensor element, and temperature dependent resistance change of sensitive layer (VOx) is measured by electronic read-out circuitry. Seek Thermal UW-AAA thermal camera (Seek Thermal Inc, USA) is employed in our work which is responsive to the radiation within 7.2-13

μm spectral region (Fig. 4.1b) (see Table 4.1 for relevant technical specifications of the camera). This spectral interval corresponds to 1389-769 cm^{-1} in wavenumber units where lies at the center of so-called fingerprint region (1500-600 cm^{-1}) of the mid-infrared spectrum (4000-400 cm^{-1}).

Table 4.1: Technical specifications of Seek Thermal camera

Model	Seek Thermal UW-AAA
Spectral region	7.2-13 μm (1389-769 cm^{-1})
Array format	206 x 156 (extrapolated to 832 x 624 pixels)
Pixel pitch	12 μm
Field of view (FoV)	36 degrees
Sampling rate	<9 Hz
Sensor technology	Vanadium Oxide Microbolometer
Mobile platform	Most Android devices running 4.3 or higher
Price	$208 (as of August 2016)

4.2.3 Silicon transmission diffraction grating

Incident radiation is dispersed by a custom-designed and fabricated transmission diffraction grating. Diffraction angle, θ_m of a transmitted order *m* is expressed by the grating equation,

$$\theta_m = \sin^{-1}\left(\frac{m\lambda}{\Lambda} + \sin\theta_i\right) \tag{4.3}$$

where λ is the wavelength of the electromagnetic wave, Λ is the period of the grating, and θ_i is the angle of incidence. A design criteria for the diffraction grating is that the whole radiation within the spectral region of interest (i.e. 7.2-13 μm) should be dispersed across the sensor array without any overlapping between the diffracted orders. According to the grating equation, setting $\Lambda = 20\,\mu m$ and $\theta_i = 30^o$ yields $\theta_{-1} = 0 \pm 8.627^o$ for $\lambda = 10 \mp 3\,\mu m$. Grating

equation serves as a useful tool for first order approach, however, it does not provide any insight on the transmission efficiencies of individual diffracted orders since it lacks the effect of surface profile. To this end, we have performed numerical calculations using a commercial software package (PCGrate) which employs modified integral method (MIM)[40]. Groove depth of a lamellar shaped grating is optimized to maximize transmission efficiency of -1st order (Fig 4.2). According to the simulation results, the groove depth, d between 1.5-2.0 μm is found to yield transmission efficiency of -1st order higher than 16% for $\lambda = 10 \mp 3\ \mu m$.

Transmission grating was fabricated out of a double side polished 200 μm thick silicon wafer (Fig. 4.2). The refractive index of Si, n_{Si}=3.418 around $\lambda = 10\ \mu m$, and silicon has no extinction within the mid-infrared region at all. One dimensional grating pattern with grating period $\Lambda = 20\ \mu m$ was defined on a wafer using optical lithography. First, a photoresist (AZ5214, AZ Electronic Materials) was spin-coated on the wafer at 4000 rpm for 45 seconds to form a thin film of mask material. Photoresist coated wafer is then prebaked at 110 C^{o} for 50 seconds. Ultraviolet (UV) radiation (60 mJ) is exposed onto the photoresist layer through a chromium mask. UV exposed regions are developed by submerging in a 1:4 diluted photoresist developer (AZ400K, AZ Electronic Materials) solution for 60 seconds. Wafer was rinsed by distilled water and dried by nitrogen gas flow. Inductively coupled plasma (ICP) etching system was used to create lamellar grooves on the wafer thanks to its high anisotropic etching characteristics. Dry etching parameters are listed on Table 4.2. Following the dry etch process, photoresist residue was removed by acetone exposure.

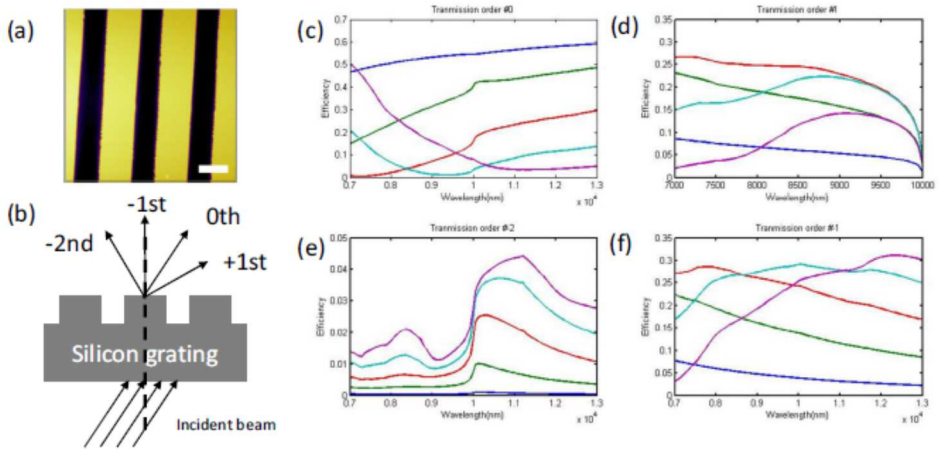

Figure 4.2: (a) AFM micrograph of microfabricated silicon diffraction grating. Groove depth, d=1.6 µm. (b) Diffracted orders for angle of incidence, $\theta_i = 30^o$ and grating period, $\Lambda = 20\ \mu m$. Only -1st diffraction order is collected by the camera lens. (c-f) Calculated transmission efficiencies of diffracted orders for varying groove depths (0.5 µm (blue), 1.0 µm (green), 1.5 µm (red), 2.0 µm (cyan), 2.5 µm (magenta)).

Table 4.2: ICP anisotropic Si etching parameters

	Deposition	**Etch**
Chamber pressure	18 mTorr	35 mTorr
Duration	5 sec	3 sec
Cycles	19	19
C_4F_8 flow rate	60 sccm	-
SF_6 flow rate	-	80 sccm
O_2 flow rate	-	10 sccm
Coil power	400 W	400 W
Platen power	0 W	10 W

4.2.4 Experimental setup

Thermal camera and transmission grating are assembled together to form a spectrometer apparatus by means of 3D-printed PLA components (Fig. 4.1b). Spectrometer apparatus is aligned to collect light at 30 degrees of angle of incidence (Fig. 4.3). Thermal camera is connected to an Android based mobile device that supports USB On-The-Go, and controlled by Seek Thermal camera application. A sample holder is placed between IR source and detector. Glow bar is electrically connected to a power supply and fed by a constant current to emit IR radiation. Spectrometer setup has no moving parts at all as opposed to the commonly used Fourier transform infrared spectroscopy (FTIR) systems, or monochromator based spectrographs. This feature enables instant spectral data generation and enhances robustness against mechanical vibrations.

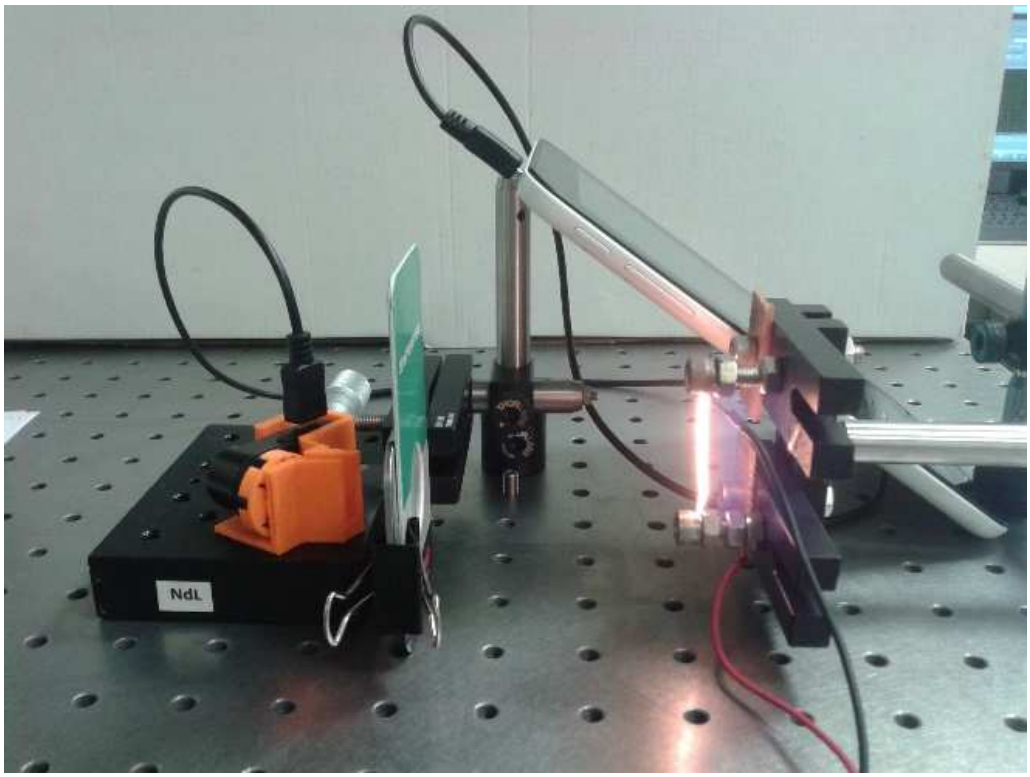

Figure 4.3: Photograph of the experimental setup

The spectroscopic data measured by the spectrometer, $g(\lambda)$ can be expressed as the sum of the linear convolution of a resolved signal $f(\lambda)$ and the point spread function (PSF) $h(\lambda)$, and a random process $n(\lambda)$,

$$g(\lambda) = f(\lambda) \otimes h(\lambda) + n(\lambda) \tag{4.4}$$

where $\otimes$ denotes the convolution operation, defined by $f(\lambda) \otimes h(\lambda) = \int f(z) \times h(\lambda - z) dz$. The PSF $h(\lambda)$ represents the overall instrumental response function which combines the line-shape function and the instrumental broadening effects.

4.3 Results and Discussion

IR absorption spectrum of a polystyrene (PS) reference standard card (76.2 μm thick) was measured using both miniaturized mid-IR spectrometer setup and Fourier transform infrared spectroscopy (FTIR) system. In the experimental setup, video recording is initiated with disabled auto-contrast settings before the placement of the polystyrene card and powering IR source. First, dark signal is taken as background spectrum ($B(\lambda)$) in the absence of IR illumination. Then, IR source is turned on and run for a few minutes to get stabilized and to minimize intensity fluctuations. Intensity signal with no sample is taken as reference spectrum ($R(\lambda)$). Finally, polystyrene card is fixed into the sample holder, and intensity signal is taken as sample spectrum ($S(\lambda)$). Transmittance spectrum, $T(\lambda)$ is calculated by,

$$T(\lambda) = \frac{S(\lambda) - B(\lambda)}{R(\lambda) - B(\lambda)}. \tag{4.5}$$

Reference, sample and transmittance spectrum images are shown in Fig. 4.4a. In order to enhance the signal-to-noise ratio, video data is averaged over time by taking the average of successive 100 frames. In addition to time averaging,

spectrum signal is averaged along the vertical axis by taking the average of 50 horizontal lines within the red colored rectangular region of interest (Fig. 4.4a). The pixel resolution of the system as defined by the ratio of spectral span to the number of actual bolometer pixel elements is found as 62 nm/pixel.

Ground-truth IR transmittance spectrum of the polystyrene card is measured using FTIR system. FTIR transmittance spectrum ($f(\lambda)$) is shown in Fig. 4.4b. The PSF $h(\lambda)$ of the experimental setup is estimated to be Gaussian function,

$$h(\lambda) = \frac{1}{\sqrt{2\pi}\sigma} exp\left(-\frac{\lambda^2}{2\sigma^2}\right) \tag{4.6}$$

where σ is the standard deviation. The standard deviation, σ is taken as 0.13 μm which gives the maximum likelihood between the measured spectrum ($g(\lambda)$) and blurred FTIR spectrum ($f(\lambda) \otimes h(\lambda)$). Agreement between the normalized measured and blurred FTIR spectra is as seen in Fig. 4.4c.

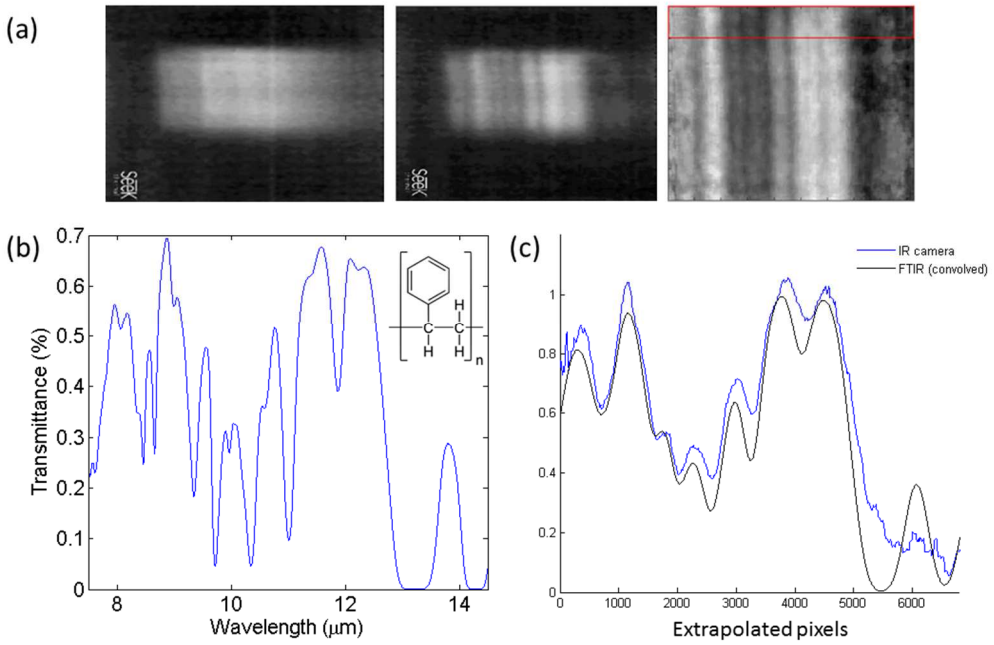

Figure 4.4: (a) Reference, sample, and transmittance spectrum images of polystyrene reference standard. (from left to right) (b) Ground truth FTIR transmittance spectrum of polystyrene reference standard. (c) Agreement between the IR camera and blurred FTIR spectra.

Extraction of the original spectrum ($f(\lambda)$) from the measured spectrum ($g(\lambda)$) requires more advanced numerical techniques so-called blind deconvolution methods [72]–[74]. In this work, we have utilized commercially available methods provided by MATLAB programming environment. "*deconvblind*" method has been performed to obtain original spectrum by a series of trial-and-error set parameter optimization. As shown in Fig. 4.5, transmittance peak positions and peak depths are in agreement with FTIR spectrum to some degree of precision. Agreement between the spectra is promising for the identification of chemical substances based on their fingerprint spectra. It is plausible to assert that both qualitative and quantitative spectroscopic analysis are achievable by incorporating well-optimized data processing and analysis approaches.

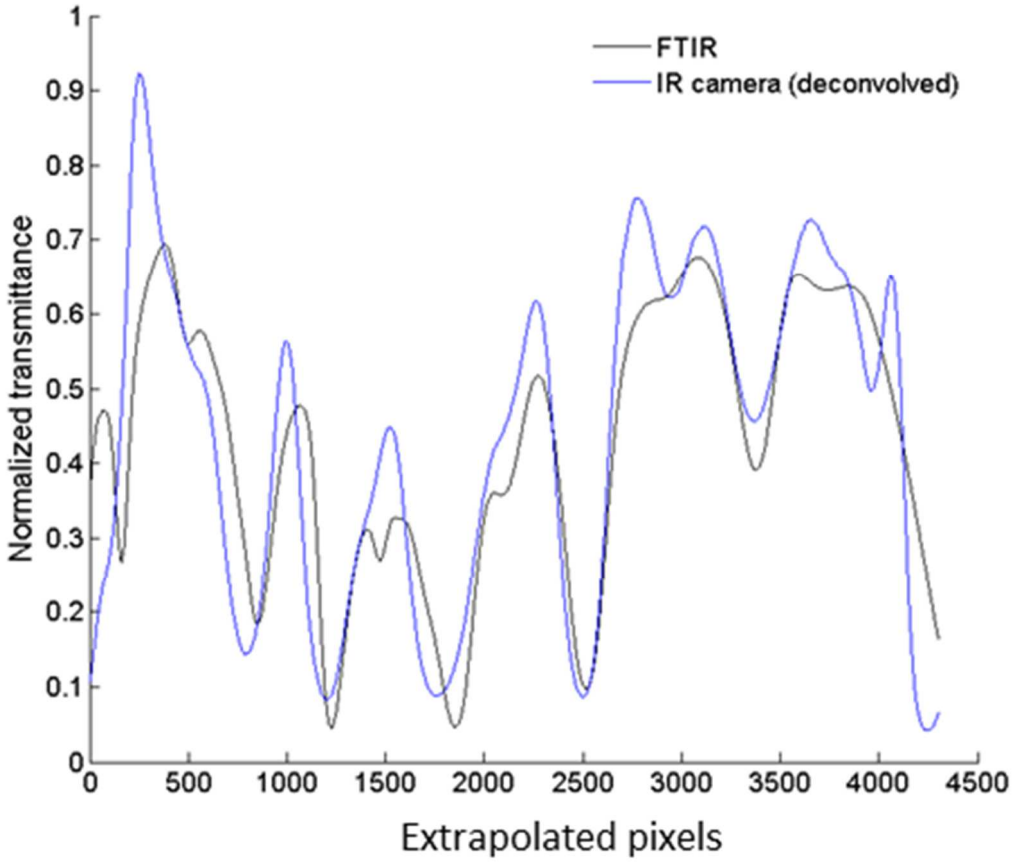

Figure 4.5: Blind deconvolution of the IR camera spectrum.

4.4 Conclusion

In this work, we demonstrated the possibility of infrared absorption spectroscopy outside the laboratory settings through integration of a miniature uncooled thermal camera and custom designed transmission grating. Our approach yielded a low cost and light weight mid-infrared spectrometer with promising precision and fast response. The optical apparatus can be utilized for analysis of a wide range of chemicals in remote or resource-limited settings from medical to environmental applications.

Chapter 5
Conclusion

We have demonstrated a sensitive and easy-to-fabricate integrated refractometric sensor design combining a biharmonic grating-coupled surface plasmon resonance (SPR) surface with a planar silicon photodiode. We have investigated plasmon enhanced transmission (PET) through periodically corrugated metallic surfaces based on analytical derivations and numerical calculations. An optimal biharmonic grating surface has been numerically found to have 30 nm grating depth and 45 nm thick Ag layer on top of a dielectric substrate with refractive index, n_s=1.45, given the grating period $\Lambda = 740\,nm$, the illumination wavelength $\lambda_i = 632.8\,nm$ and the refractive index of the sensing medium n_d=1.33. Theoretical refractive index sensitivities were calculated as 50 ^{o}/RIU and 81 ^{o}/RIU for the 1st and 2nd order resonances, respectively. Integration of grating-coupled SPR surface with a custom-fabricated silicon photodiode substrate was realized through nanoimprint lithography and thin film metallization processes. Refractive index sensing experiments have been conducted by streaming distilled water and NaCl solutions through the fluidic channel mounted on the sensor device and monitoring photocurrent in real-time. Experimental refractive index sensitivities have been found as 91 ^{o}/RIU and 83 ^{o}/RIU for the 1st and 2nd order resonances, respectively. The discrepancy between the theoretical and experimental sensitivities was attributed to systemic measurement errors of the resonance angles in our setup. Refractive index noise was found as 6.3 x 10^{-6}

$RIU/\sqrt{Hz}$, compared to a shot-noise limited RI noise of 5.61 x 10^{-9} $RIU/\sqrt{Hz}$, due to laser source noise dominated experimental configuration. In order to improve the sensitivity, we have demonstrated balanced detection scheme which yielded 5-fold enhancement, resulting RI noise of 1.2 x 10^{-6} $RIU/\sqrt{Hz}$. Our approach yielded a low cost and sensitive SPR sensor with high level of miniaturization which can find applications in integrated lab-on-a-chip (LOC) designs.

We have realized surface plasmon resonance imaging (SPRi) on a smartphone for the first time by developing a compact optical attachment together with Ag/Au bimetallic grating surfaces through the modification of Blu-ray discs. The hand-held SPRi platform features the capability of measuring time-resolved intensity modulated SPR signals from over 20.000 individual pixels with 12 $\mu m/pixel$ spatial resolution, simultaneously. Blu-ray discs were converted to planar and disposable plasmonic sensor surfaces by physical procedures and thin film metallization. A numerically optimized Ag/Au bilayer grating structure has been employed to operate in aqueous analyte medium under normal incidence of illumination at the central region of the visible spectrum while maintaining sensitivity, chemical stability and biological affinity. Sensitivity performance of the system has been investigated both numerically and experimentally. The experimental spectral bulk refractive index sensitivity, $S_{\lambda BE}$ has been found as 356 nm/RIU in good agreement with the calculated spectral bulk refractive index sensitivity, $S_{\lambda BC}$=316 nm/RIU. SPR difference images of an Ag/Au microspot array were taken covering over 50 circular spots having 110 μm diameter each with low intra-sensor variability. Glycerol solution exposure experiments have shown that the experimental reflectivity bulk refractive index sensitivity, S_{RBE} is 485 %/RIU whereas the dynamic range is as wide as 22200 x 10^{-6} RIU with high linearity (R^2=0.9951). The reflectivity noise, σ_R has been reduced down to 0.02% by time and area averaging that yielded the minimum detectable bulk refractive index change, σ_n as 4.12 x 10^{-5} RIU which is comparable with the detection

performance of commercial benchtop analyzers. Biodetection performance has been investigated by monitoring bovine serum albumin (BSA) adsorption and performing rabbit anti mouse (RAM) IgG - mouse IgG assay. Formation of BSA monolayer on the sensor surface has been tracked in real-time with signal-to-noise ratio of 218. The experimental spectral surface coating sensitivity, $S_{\lambda SE}$ was estimated to be between 0.46-0.8 nm/nm which is in good agreement with the calculated spectral surface coating sensitivity, $S_{\lambda SC}$=0.7 nm/nm. As an exemplary selective biomolecular binding experiment, capture of mouse IgG by immobilized layer of RAM IgG was implemented in direct assay fashion. Sigmoidal dose-response curve obtained within 1.33 nM - 830 nM concentration range revealed that nanomolar level detection of antibody analyte is realizable. Our approach in miniaturization of SPR biosensing could pave the way towards application of cost-effective parallel assays and multi-analyte detection for point-of-care testing.

We have demonstrated infrared absorption spectroscopy on a mobile phone by developing a compact dispersive mid-IR spectrometer that hosts a miniature uncooled thermal camera and custom-designed silicon transmission diffraction grating. The spectrometer operates within 7.2-13 μm (1389-769 cm^{-1}) spectral range located at the center of fingerprint region. A numerically optimized lamellar transmission grating has been calculated to have 1st order transmission efficiency greater than 16% for grating depth, *d* between 1.5-2.0 μm with a narrow diffraction angle span $\theta_{-1} = 0 \pm 8.627^{o}$ for incident radiation wavelength range $\lambda = 10 \mp 3\ \mu m$ setting grating period, $\Lambda = 20\ \mu m$ and the angle of incidence $\theta_i = 30^{o}$. Silicon grating having grating depth, *d*=1.6 μm was microfabricated through UV optical lithography and inductively coupled plasma (ICP) etching processes. Proof-of-concept experiments have been conducted by measuring transmittance spectra of a polystyrene film with both spectrometer apparatus and Fourier transform infrared spectroscopy (FTIR) system. Experimental results have been found to be in good agreement. The pixel resolution of the device was calculated as 62 nm/pixel, and the point spread function (PSF) of the overall system was estimated to have a Gaussian form with the standard deviation, σ=0.13

μm. Our approach yielded a mobile phone controlled miniaturized mid-IR spectrometer which can be utilized for the analysis of a wide range of chemicals in the field settings.

Bibliography

[1] C. D. Chin, V. Linder, and S. K. Sia, “Commercialization of microfluidic point-of-care diagnostic devices,” *Lab Chip*, vol. 12, no. 12, pp. 2118–2134, 2012.

[2] A. M. Foudeh, T. Fatanat Didar, T. Veres, and M. Tabrizian, “Microfluidic designs and techniques using lab-on-a-chip devices for pathogen detection for point-of-care diagnostics,” *Lab Chip*, vol. 12, no. 18, pp. 3249–3266, 2012.

[3] J. Homola, “Surface plasmon resonance sensors for detection of chemical and biological species.,” *Chem. Rev.*, vol. 108, no. 2, pp. 462–93, Feb. 2008.

[4] B. Liedberg, C. Nylander, and I. Lunström, “Surface plasmon resonance for gas detection and biosensing,” *Sensors and Actuators*, vol. 4, pp. 299–304, Jan. 1983.

[5] J. Homola, “Present and future of surface plasmon resonance biosensors,” *Anal. Bioanal. Chem.*, vol. 377, no. 3, p. 528—539, 2003.

[6] J. Homola, S. S. Yee, and G. Gauglitz, “Surface plasmon resonance sensors: review,” *Sensors Actuators B Chem.*, vol. 54, no. 1–2, pp. 3–15, Jan. 1999.

[7] F.-C. Chien and S.-J. Chen, “A sensitivity comparison of optical biosensors based on four different surface plasmon resonance modes,” *Biosens. Bioelectron.*, vol. 20, no. 3, pp. 633–642, 2004.

[8] J. Homola, I. Koudela, and S. S. Yee, “Surface plasmon resonance sensors based on diffraction gratings and prism couplers: sensitivity

comparison," *Sensors Actuators B Chem.*, vol. 54, no. 1–2, pp. 16–24, Jan. 1999.

[9] K. Matsubara, S. Kawata, and S. Minami, "Optical chemical sensor based on surface plasmon measurement," *Appl. Opt.*, vol. 27, no. 6, pp. 1160–1163, Mar. 1988.

[10] J. Dostálek, J. Homola, and M. Miler, "Rich information format surface plasmon resonance biosensor based on array of diffraction gratings," *Sensors Actuators B Chem.*, vol. 107, no. 1, pp. 154–161, May 2005.

[11] F. Eftekhari, R. Gordon, J. Ferreira, A. G. Brolo, and D. Sinton, "Polarization-dependent sensing of a self-assembled monolayer using biaxial nanohole arrays," *Appl. Phys. Lett.*, vol. 92, no. 25, p. 253103, 2008.

[12] K. M. Mayer and J. H. Hafner, "Localized surface plasmon resonance sensors.," *Chem. Rev.*, vol. 111, no. 6, pp. 3828–57, Jun. 2011.

[13] S. A. Kim and S. B. Jun, "In-vivo Optical Measurement of Neural Activity in the Brain," *Exp. Neurobiol.*, vol. 22, no. 3, pp. 158–166, Sep. 2013.

[14] Y. Liu, Q. Liu, S. Chen, F. Cheng, H. Wang, and W. Peng, "Surface Plasmon Resonance Biosensor Based on Smart Phone Platforms," *Sci. Rep.*, vol. 5, p. 12864, Aug. 2015.

[15] P. J. R. Roche, S. Filion-Côté, M. C.-K. Cheung, V. P. Chodavarapu, and A. G. Kirk, "A Camera Phone Localised Surface Plasmon Biosensing Platform towards Low-Cost Label-Free Diagnostic Testing," *J. Sensors*, vol. 2011, pp. 1–7, 2011.

[16] X. D. Hoa, A. G. Kirk, and M. Tabrizian, "Towards integrated and sensitive surface plasmon resonance biosensors: A review of recent progress," *Biosensors and Bioelectronics*, vol. 23, no. 2. pp. 151–160, 2007.

[17] A. Otto, "Excitation of nonradiative surface plasma waves in silver by the method of frustrated total reflection," *Zeitschrift für Phys.*, vol. 216, no. 4, pp. 398–410, 1968.

[18] E. Kretschmann, “Die Bestimmung optischer Konstanten von Metallen durch Anregung von Oberfl??chenplasmaschwingungen,” *Zeitschrift für Phys.*, vol. 241, no. 4, pp. 313–324, 1971.

[19] J. van Gent, P. V Lambeck, H. J. Kreuwel, G. J. Gerritsma, E. J. Sudhölter, D. N. Reinhoudt, and T. J. Popma, “Optimization of a chemooptical surface plasmon resonance based sensor.,” *Appl. Opt.*, vol. 29, no. 19, pp. 2843–2849, 1990.

[20] M. L. Dakss, L. Kuhn, P. F. Heidrich, and B. A. Scott, “Grating coupler for efficient excitation of optical guided waves in thin films,” *Appl. Phys. Lett.*, vol. 16, no. 12, pp. 523–525, 1970.

[21] M. Piliarik, M. Vala, I. Tichy, and J. Homola, “Compact and low-cost biosensor based on novel approach to spectroscopy of surface plasmons,” *Biosens Bioelectron*, vol. 24, no. 12, pp. 3430–3435, 2009.

[22] E. Ouellet, C. Lausted, T. Lin, C. W. T. Yang, L. Hood, and E. T. Lagally, “Parallel microfluidic surface plasmon resonance imaging arrays.,” *Lab Chip*, vol. 10, no. 5, pp. 581–8, 2010.

[23] K. Gurel, B. Kaplan, H. Guner, M. Bayindir, and A. Dana, “Resonant transmission of light through surface plasmon structures,” *Appl. Phys. Lett.*, vol. 94, no. 23, p. 233102, 2009.

[24] L. Salomon, F. Grillot, A. V Zayats, and F. de Fornel, “Near-field distribution of optical transmission of periodic subwavelength holes in a metal film.,” *Phys. Rev. Lett.*, vol. 86, no. 6, pp. 1110–3, Feb. 2001.

[25] H. Lezec and T. Thio, “Diffracted evanescent wave model for enhanced and suppressed optical transmission through subwavelength hole arrays.,” *Opt. Express*, vol. 12, no. 16, pp. 3629–3651, 2004.

[26] U. Schröter and D. Heitmann, “Surface-plasmon-enhanced transmission through metallic gratings,” *Phys. Rev. B*, vol. 58, no. 23, pp. 15419–15421, 1998.

[27] L. Pang, G. M. Hwang, B. Slutsky, and Y. Fainman, “Spectral sensitivity of two-dimensional nanohole array surface plasmon polariton resonance sensor,” *Appl. Phys. Lett.*, vol. 91, no. 12, p. 123112, 2007.

[28] A. Lesuffleur, H. Im, N. C. Lindquist, and S.-H. Oh, “Periodic nanohole arrays with shape-enhanced plasmon resonance as real-time biosensors,” *Appl. Phys. Lett.*, vol. 90, no. 24, p. 243110, 2007.

[29] T. W. Ebbesen, H. J. Lezec, H. F. Ghaemi, T. Thio, and P. A. Wolff, “Extraordinary optical transmission through sub-wavelength hole arrays,” *Nature*, vol. 391, no. 6668, pp. 667–669, 1998.

[30] A. Pipino, R. Van Duyne, and G. Schatz, “Surface-enhanced second-harmonic diffraction: Experimental investigation of selective enhancement,” *Phys. Rev. B*, vol. 53, no. 7, pp. 4162–4169, 1996.

[31] P. Adam, J. Dostálek, O. Telezhnikova, and J. Homola, “SPR Sensor Based on a Bi-diffractive Grating,” in *Proc. SPIE*, 2007, p. Vol 6585, 65851Y.

[32] A. Kocabas, S. Seckin Senlik, and A. Aydinli, “Plasmonic band gap cavities on biharmonic gratings,” *Phys. Rev. B*, vol. 77, no. 19, p. 195130, May 2008.

[33] C. Neipp, a Beléndez, S. Gallego, M. Ortuño, I. Pascual, and J. Sheridan, “Angular responses of the first and second diffracted orders in transmission diffraction grating recorded on photopolymer material.,” *Opt. Express*, vol. 11, no. 16, pp. 1835–1843, 2003.

[34] H. J. Simon, D. E. Mitchell, and J. G. Watson, “Optical second-harmonic generation with surface plasmons in silver films,” *Phys. Rev. Lett.*, vol. 33, no. 26, pp. 1531–1534, 1974.

[35] J. Homola, *Surface Plasmon Resonance Based Sensors*. Springer Berlin Heidelberg, 2006.

[36] O. O. Ekiz, K. Mizrak, and A. Dâna, “Chemically specific dynamic characterization of photovoltaic and photoconductivity effects of surface nanostructures.,” *ACS Nano*, vol. 4, no. 4, pp. 1851–60, Apr. 2010.

[37] A. Kocabas, A. Da^na, and A. Aydinli, “Excitation of a surface plasmon with an elastomeric grating,” *Appl. Phys. Lett.*, vol. 89, no. 4, p. 041123, 2006.

[38] A. Kocabas, F. Ay, A. Dâna, and A. Aydinli, “An elastomeric grating

coupler," *J. Opt. A Pure Appl. Opt.*, vol. 8, no. 1, pp. 85–87, Jan. 2006.

[39] B. Kaplan, H. Guner, O. Senlik, K. Gurel, M. Bayindir, and A. Dana, "Tuning Optical Discs for Plasmonic Applications," *Plasmonics*, vol. 4, no. 3, pp. 237–243, 2009.

[40] I. International Intellectual Group, "PCGrate-S." 2011.

[41] F. Romanato, K. H. Lee, H. K. Kang, G. Ruffato, and C. C. Wong, "Sensitivity enhancement in grating coupled surface plasmon resonance by azimuthal control.," *Opt. Express*, vol. 17, no. 14, pp. 12145–12154, 2009.

[42] K. H. Lee, F. Romanato, H. K. Kang, and C. C. Wong, "Polarization optimization for a full sensitivity in azimuthal grating coupled surface plasmon resonance," *Sensors Actuators B Chem.*, vol. 148, no. 1, pp. 181–185, Jun. 2010.

[43] S. K. Vashist, O. Mudanyali, E. M. Schneider, R. Zengerle, and A. Ozcan, "Cellphone-based devices for bioanalytical sciences Multiplex Platforms in Diagnostics and Bioanalytics," *Anal. Bioanal. Chem.*, vol. 406, no. 14, pp. 3263–3277, 2014.

[44] Y. Lu, W. Shi, J. Qin, and B. Lin, "Low cost, portable detection of gold nanoparticle-labeled microfluidic immunoassay with camera cell phone.," *Electrophoresis*, vol. 30, no. 4, pp. 579–82, Feb. 2009.

[45] O. Mudanyali, S. Dimitrov, U. Sikora, S. Padmanabhan, I. Navruz, and A. Ozcan, "Integrated rapid-diagnostic-test reader platform on a cellphone.," *Lab Chip*, vol. 12, no. 15, pp. 2678–86, 2012.

[46] D. N. Breslauer, R. N. Maamari, N. A. Switz, W. A. Lam, and D. A. Fletcher, "Mobile phone based clinical microscopy for global health applications.," *PLoS One*, vol. 4, no. 7, p. e6320, Jan. 2009.

[47] H. Zhu, S. Mavandadi, A. F. Coskun, O. Yaglidere, and A. Ozcan, "Optofluidic fluorescent imaging cytometry on a cell phone.," *Anal. Chem.*, vol. 83, no. 17, pp. 6641–7, Sep. 2011.

[48] L. Shen, J. a. Hagen, and I. Papautsky, "Point-of-care colorimetric detection with a smartphone," *Lab Chip*, vol. 12, no. 21, p. 4240, 2012.

[49] D. Gallegos, K. D. Long, H. Yu, P. P. Clark, Y. Lin, S. George, P. Nath, and B. T. Cunningham, “Label-free biodetection using a smartphone.,” *Lab Chip*, vol. 13, no. 11, pp. 2124–32, Jun. 2013.

[50] P. Preechaburana, M. C. Gonzalez, A. Suska, and D. Filippini, “Surface plasmon resonance chemical sensing on cell phones.,” *Angew. Chem. Int. Ed. Engl.*, vol. 51, no. 46, pp. 11585–8, Nov. 2012.

[51] K. Bremer and B. Roth, “Fibre optic surface plasmon resonance sensor system designed for smartphones.,” *Opt. Express*, vol. 23, no. 13, pp. 17179–84, 2015.

[52] S. Dutta, K. Saikia, and P. Nath, “Smartphone based LSPR sensing platform for bio-conjugation detection and quantification,” *RSC Adv.*, vol. 6, no. 26, pp. 21871–21880, Feb. 2016.

[53] B. H. Ong, X. Yuan, S. C. Tjin, J. Zhang, and H. M. Ng, “Optimised film thickness for maximum evanescent field enhancement of a bimetallic film surface plasmon resonance biosensor,” *Sensors Actuators, B Chem.*, vol. 114, no. 2, pp. 1028–1034, 2006.

[54] L. Xia, S. Yin, H. Gao, Q. Deng, and C. Du, “Sensitivity Enhancement for Surface Plasmon Resonance Imaging Biosensor by Utilizing Gold--Silver Bimetallic Film Configuration,” *Plasmonics*, vol. 6, no. 2, pp. 245–250, 2011.

[55] Y. Chen, R. S. Zheng, D. G. Zhang, Y. H. Lu, P. Wang, H. Ming, Z. F. Luo, and Q. Kan, “Bimetallic chips for a surface plasmon resonance instrument.,” *Appl. Opt.*, vol. 50, no. 3, pp. 387–91, 2011.

[56] C. T. Li, K. C. Lo, H. Y. Chang, H. T. Wu, J. H. Ho, and T. J. Yen, “Ag/Au bi-metallic film based color surface plasmon resonance biosensor with enhanced sensitivity, color contrast and great linearity,” *Biosens. Bioelectron.*, vol. 36, no. 1, pp. 192–198, 2012.

[57] B. Turker, H. Guner, S. Ayas, O. O. Ekiz, H. Acar, M. O. Guler, and A. Dâna, “Grating coupler integrated photodiodes for plasmon resonance based sensing.,” *Lab Chip*, vol. 11, no. 2, pp. 282–7, Jan. 2011.

[58] E. D. Palik, *Handbook of Optical Constants of Solids*, vol. 1. 1985.

[59] S. H. Ahn and L. J. Guo, “High-Speed Roll-to-Roll Nanoimprint Lithography on Flexible Plastic Substrates,” *Adv. Mater.*, vol. 20, no. 11, pp. 2044–2049, Jun. 2008.

[60] G. G. Nenninger, M. Piliarik, and J. Homola, “Data analysis for optical sensors based on spectroscopy of surface plasmons,” *Meas. Sci. Technol.*, vol. 13, no. 12, pp. 2038–2046, Dec. 2002.

[61] D. C. Cullen, R. G. W. Brown, and C. R. Lowe, “Detection of immuno-complex formation via surface plasmon resonance on gold-coated diffraction gratings,” *Biosensors*, vol. 3, no. 4, pp. 211–225, Jan. 1987.

[62] C. Nylander, B. Liedberg, and T. Lind, “Gas detection by means of surface plasmon resonance,” *Sensors and Actuators*, vol. 3, pp. 79–88, Jan. 1982.

[63] Z. Wang, Z. Cheng, V. Singh, Z. Zheng, Y. Wang, S. Li, L. Song, and J. Zhu, “Stable and sensitive silver surface plasmon resonance imaging sensor using trilayered metallic structures.,” *Anal. Chem.*, vol. 86, no. 3, pp. 1430–6, Feb. 2014.

[64] L. Song, Z. Wang, D. Zhou, A. Nand, S. Li, B. Guo, Y. Wang, Z. Cheng, W. Zhou, Z. Zheng, and J. Zhu, “Waveguide coupled surface plasmon resonance imaging measurement and high-throughput analysis of bio-interaction,” *Sensors Actuators B Chem.*, vol. 181, pp. 652–660, May 2013.

[65] D. C. Carter and J. X. Ho, “Structure of serum albumins,” *Adv. Protein Chem.*, vol. 45, pp. 153–203, 1994.

[66] J. M. Chalmers and P. R. Griffiths, *Handbook of Vibrational Spectroscopy*. Wiley, 2001.

[67] M. Yaman, A. Yildirim, M. Kanik, T. C. Cinkara, and M. Bayindir, “High selectivity Boolean olfaction using hollow-core wavelength-scalable Bragg fibers.,” *Anal. Chem.*, vol. 84, no. 1, pp. 83–90, Jan. 2012.

[68] A. Yildirim, F. E. Ozturk, and M. Bayindir, “Smelling in chemically complex environments: an optofluidic Bragg fiber array for differentiation of methanol adulterated beverages.,” *Anal. Chem.*, vol. 85, no. 13, pp.

6384–91, Jul. 2013.

[69] C. Corsi, A. Dundee, P. Laurenzi, N. Liberatore, D. Luciani, S. Mengali, A. Mercuri, A. Pifferi, M. Simeoni, G. Tosone, R. Viola, and D. Zintu, “Chemical Warfare Agents Analyzer Based on Low Cost, Room Temperature, and Infrared Microbolometer Smart Sensors,” *Adv. Opt. Technol.*, vol. 2012, pp. 1–5, 2012.

[70] “Seek Thermal, Inc.” [Online]. Available: http://www.thermal.com/. [Accessed: 01-Aug-2016].

[71] “FLIR Systems, Inc.” [Online]. Available: http://www.flir.com/flirone/. [Accessed: 01-Aug-2016].

[72] L. Z. Deng, L. Cao, and H. Zhu, “Spectral semi-blind deconvolution with hybrid regularization,” *Infrared Phys. Technol.*, vol. 64, pp. 91–96, 2014.

[73] H. Liu, Z. Zhang, S. Liu, J. Shu, T. Liu, L. Yan, and T. Zhang, “Spectral blind deconvolution with differential entropy regularization for infrared spectrum,” *Infrared Phys. Technol.*, vol. 71, pp. 481–491, 2015.

[74] H. Liu, M. Zhou, Z. Zhang, J. Shu, T. Liu, and T. Zhang, “Multi-order blind deconvolution algorithm with adaptive Tikhonov regularization for infrared spectroscopic data,” *Infrared Phys. Technol.*, vol. 71, pp. 63–69, 2015.

Appendix A

Publications in SCI journals

9. H. Guner, E. Ozgur, G. Kokturk, M. Celik, E. Esen, A.E. Topal, S. Ayas, Y. Uludag, C. Elbuken and A. Dana, "A smartphone based surface plasmon resonance imaging (SPRi) platform for on-site biodetection", *Sensors and Actuators B: Chemical* 239, 571-577, 2017.

8. S. Ayas, A.E. Topal, A. Cupallari, H Guner, G. Bakan, A. Dana, "Exploiting Native Al2O3 for Multispectral Aluminum Plasmonics", *ACS Photonics* 1(12), 1313–1321, 2014.

7. Y. Kaya, S. Ayas, A.E. Topal, H. Guner, A. Dana, "Sensitivity comparison of localized plasmon resonance structures and prism coupler", *Sensors and Actuators B: Chemical* 191, 516-521, 2014.

6. S. Ayas, H. Guner, G. Turker, O.O. Ekiz, F. Dirisaglik, A.K. Okyay and A. Dana, "Raman Enhancement on a Broadband Meta-Surface", *ACS Nano* 6(8), 6852-6861, 2012.

5. U. Kurum, O. O. Ekiz, H. G. Yaglioglu, A. Elmali, M. Urel, H. Guner, A. K. Mizrak, B. Ortac and A. Dana, "Electrochemically tunable ultrafast optical response of graphene oxide", *Applied Physics Letters* 98, 141103, 2011.

4. O. O. Ekiz, M. Urel, H. Guner, A. K. Mizrak and A. Dana, "Reversible Electrical Reduction and Oxidation of Graphene Oxide", *ACS Nano* 5, 2475, 2011.

3. B. Turker, H. Guner, S. Ayas, O. O. Ekiz, H. Acar, M. O. Guler and A. Dana, “Grating coupler integrated photodiodes for plasmon resonance based sensing”, *Lab Chip* 11, 282, 2011.

2. K. Gurel, B. Kaplan, H. Guner, M. Bayindir and A. Dana, “Resonant transmission of light through surface plasmon structures”, *Applied Physics Letters* 94, 233102, 2009.

1. B. Kaplan, H. Guner, O. Senlik, K. Gurel, M. Bayindir and A. Dana, “Tuning Optical Discs for Plasmonic Applications”, *Plasmonics* 4, 237, 2009.